IMAGING UNDER RUGGED TOPOGRAPHY AND COMPLEX VELOCITY STRUCTURE

A DISSERTATION
SUBMITTED TO THE DEPARTMENT OF GEOPHYSICS
AND THE COMMITTEE ON GRADUATE STUDIES
OF STANFORD UNIVERSITY
IN PARTIAL FULFILLMENT OF THE REQUIREMENTS
FOR THE DEGREE OF
DOCTOR OF PHILOSOPHY

By
Dimitri Bevc
August 1995

printed as Stanford Exploration Project No. 87
by permission of the author

I certify that I have read this thesis and that in my opinion it is fully adequate, in scope and in quality, as a dissertation for the degree of Doctor of Philosophy.

Jon F. Claerbout (Principal Advisor)

I certify that I have read this thesis and that in my opinion it is fully adequate, in scope and in quality, as a dissertation for the degree of Doctor of Philosophy.

Francis Muir

I certify that I have read this thesis and that in my opinion it is fully adequate, in scope and in quality, as a dissertation for the degree of Doctor of Philosophy.

Norman Sleep

I certify that I have read this thesis and that in my opinion it is fully adequate, in scope and in quality, as a dissertation for the degree of Doctor of Philosophy.

Gregory Beroza

Approved for the University Committee on Graduate Studies:

Imaging under rugged topography and complex velocity structure

Dimitri Bevc, Ph.D.
Stanford University, 1995

ABSTRACT

I demonstrate how wave-equation datuming can be applied to improve imaging in two of the most challenging environments facing geophysicists: overthrust areas with substantial surface topography and areas of complex velocity structure. I look at these challenges from the point of view that problems arise because the data have not been collected at the ideal recording surface. In the case of overthrust data, problems occur because data are collected along an irregularly sampled rugged surface. In the case of complex velocity structure, problems occur because the data are recorded too far away from the imaging target.

I compare Kirchhoff, phase-shift and finite-difference wave-equation datuming operators by formulating them as adjoint operators and casting them in a unified theoretical framework. This, and a series of synthetic examples allows me to compare and contrast the three different methods. The evaluation leads me to conclude that the Kirchhoff method is best because it is the the most efficient method for application to prestack data, and it can be easily applied to three-dimensional data. Furthermore, the Kirchhoff implementation handles the exact topographic elevations, and its application is not confined to a regular computational grid.

When data are distorted by rugged acquisition topography, I apply wave-equation datuming early in the processing flow to upward continue the data to a flat datum. This approach does not require a detailed a priori knowledge of the near-surface velocity, and it streamlines subsequent processing because the data are regridded onto a regularly sampled datum. Wave-equation datuming unravels the distortions caused by rugged topography, and unlike the static shift method, it does not adversely effect subsequent wave-based processing. The image obtained after wave-equation datuming exhibits better reflector

continuity and more accurately represents the true structural image than the image obtained after static shift.

To image complex structures, I develop a hybrid datuming and migration algorithm which is based on breaking up the complex velocity structure into small regions where first-arrival traveltimes are well behaved and coincide with the most energetic arrivals. The traveltimes are used first for imaging, and second for downward continuation of the entire survey to the boundary of the next region. Because traveltimes are computed for small depth domains, the adverse effects of caustics, headwaves, and multiple arrivals do not develop. This results in images comparable to those obtained by shot-profile migration, and superior to those created using maximum-amplitude traveltimes and band-limited traveltimes.

Approved for publication:

By ______________________________

For Department of Geophysics

Preface

All of the figures in this thesis are marked with one of three labels, [R] [NR] or [CR]. These define whether the figure is reproducible from the information provided on the CD-ROM version of this thesis.

If a figure is marked with an [R] it should be fully reproducible. All of the input data and source files required to create the figure are provided on the CD. The postscript file containing the figure can be removed and the cakefile rules provided on the CD should rebuild the figure on any of the supported computer architectures.

If a figure is marked with a [CR] it is conditionally reproducible. All the data and source files are provided on the CD but some particular environment may be necessary to recreate the figure. Many figures in this thesis were created using programs that run on a Thinking Machines Co. CM-5 computer. If the code that is provided will only compile on a CM-5 then the figure will be marked as conditionally reproducible.

If a figure is marked with an [NR] it is non reproducible. It cannot be recreated from the data on the CD. The figure may have been created by means of a commercial software product, or by means of software written by another author that is not available on the CD. It may be a hand drawn figure or a figure for which the commands to recreate it are not available. In all of these cases, if you remove the postscript file of the figure, there is no way to recreate it.

All of the reproducible and conditionally reproducible figures contain a button in the caption. Clicking with the center mouse button will bring up a panel that allows you to interact with the figure. You can display the figure in a separate window or destroy and rebuild the figure. If the figure is conditionally reproducible, you can view the warning message that tells you under what conditions the figure can be rebuilt. If the figure caption is followed by the word *movie*, you can press the interaction button to view the movie.

Acknowledgments

I have often compared working toward a Ph.D. to climbing a big mountain. It is an onerous task with many potential rewards, but when you start out you don't know exactly where you are going and what it is going to be like. You have to put aside the fear that the mountain is too big and that the summit is too far away, and just go for it. Focus on one pitch at a time and make sure that your protection is solid so that you can keep moving up. One of my big-wall climbing partners once said that the reason we do it is that it feels so good when we stop. Well, that is true, but the summit and the journey both have great rewards.

I had a great deal of help on this particular climb, so I especially thank my advisor, Jon Claerbout, and the sponsors of the Stanford Exploration Project (SEP) for providing a unique and stimulating research and educational environment. I enjoyed my stay here and I am grateful for the opportunity that was presented to me. The guidance of the many visiting and consulting faculty, including Biondo Biondi, Stew Levin, and Francis Muir was invaluable.

Part of what makes the SEP experience so great is the interaction between students. My longtime office mate during my tenure at SEP, Mihai Popovici, not only became a friend but also provided me with many insightful discussions and ideas. He contributed greatly to the recursive datuming formulations and to the ideas about layer-stripping depth migration. Of my other office mates, Patrick Blondel provided many interesting discussions and became a good friend, and Carlos Cunha helped me learn the ropes at SEP while patiently answering my countless programming and system questions. I learned a great deal from my fellow students during seminars and informal discussions. Not only do I value all the scientific advice I got from fellow students, but I am also thankful for the system maintenance efforts that all have participated in. For both the scientific and system contributions, I owe special thanks to Jun Ji, David Lumley, Dave Nichols, Martin

Karrenbach, Lin Zhang, Steve Cole, Ray Abma, Matthias Schwab, and Gopal Palacharla.

A great benefit of SEP is the exposure that students get to the sponsors. This vital link to industry stimulates research, and motivates hard work on real-world problems. It also affords students the opportunity to gain insight and advice from experienced professionals and to get interesting data sets. The Husky–Talisman Canadian foothill data was kindly provided by Christof Stork of Advance Geophysical and the preprocessed Marmousi synthetic was provided by François Audebert of Compagnie Général de Géophysique. I thank them and the companies involved for making the data available.

I thank my parents, Dr. Vladislav and Nada Bevc, for instilling me with the desire to learn and to discover new things. Special thanks go to my wife, Mary, for her love and support during these years of graduate study. If it had not been for her encouragement, I may well not have undertaken this challenge. Now she finally gets to find out what it is like to be married to a non-student!

Table of Contents

List of Figures

Chapter 1

Introduction

A goal of reflection seismic imaging is to reduce risk in exploration and development ventures. Within that context it is used to identify and define new prospects, to extend known prospects, and to monitor exploitation activities. As society's energy demands are ever increasing, and the Earth's resources are diminishing, these exploration and development activities are being applied with greater regularity in more difficult areas. Exploration objectives are more complicated, and data acquisition, processing, and interpretation is more challenging in many of the parts of the world where the search for frontier prospects is undertaken. In many of these areas, the imaging challenge is to compensate for the effects of rugged topography properly, or to image complex structures with complex subsurface velocity distributions. Both of these effects, together and separately, present some of the greatest imaging challenges to geophysicists.

In this dissertation, I investigate two of the most complicated factors affecting reflection seismic structural imaging: the effects of rugged acquisition topography, and complex velocity structure. When these effects are present, standard processing, imaging, and velocity estimation methods often fail. The reason they fail is that most standard methods are based on certain simplifying assumptions that may not be valid under the given circumstances.

I present methods based on wavefield extrapolation that result in improved imaging in regions of rugged topography and complex velocity structure. The two major contributions that I present in this dissertation are

- A method of applying wave-equation datuming to land data without detailed knowledge of the near-surface velocity structure. This simplifies subsequent processing steps and allows near-surface velocity to be estimated as part of the standard processing flow. Using a real data example, I show where wave-equation datuming fits into the processing sequence for land data with rugged acquisition topography.

- An efficient layer-stripping Kirchhoff migration algorithm that produces excellent imaging results using first-arrival traveltimes from a finite-difference solution to the eikonal equation.

1.1 Redatuming to improve processing and imaging

The failure of standard processing and imaging methods in complex areas can be thought of as arising from the fact that the data have not been collected at the ideal recording datum. In the case of land data, the failure can occur when data have been collected along an irregularly-sampled rugged surface, not on a level and regular grid. In the case of complex velocity structure, the problem can occur because the data have been recorded too far away from the imaging target, and not at the ideal subsurface location.

Under certain conditions the rugged topography problem can be compensated for by redatuming with static shift; however, when the assumptions behind the static correction are invalid, subsequent processing and imaging is degraded. Alternatively, the data can be processed from a nonflat datum, but this requires special algorithms that can accommodate irregular and rugged geometry. This can be a problem because most algorithms are optimized for regularly-sampled data referenced to a flat datum. If the data are referenced to a flat datum, structures are not distorted by topography, and interpreter input is facilitated both in the processing and imaging stages.

To ameliorate these problems in areas of rugged topography, I apply wave-equation datuming to transform the data to an ideal, regularly sampled, flat datum. This is the most accurate method of redatuming because it preserves the wavefield nature of the data and thus does not adversely affect subsequent wave-equation processing steps. Another advantage of wave-equation datuming over static shifts is that it is capable of regridding the data to a regular computational mesh. Once the data are redatumed, a wide range of processing algorithms can be applied. There is no restriction imposing the use of specialized algorithms that can handle nonflat irregular geometry. Once the data are properly redatumed, incorporation of geological information in velocity model building and assessment of processing validity is easier because structures are readily identified and correctly interpreted.

In areas of complex velocity structure, the migration result is improved if the data are downward continued through complex overlying structures, and the imaging is performed from a datum that is closer to the target zone. In this way, the deleterious effects of complex overburden are stripped away. The greatest benefit of this layer-stripping approach is that the complex velocity model is broken up into smaller portions. This is a great benefit for Kirchhoff imaging methods which employ summation trajectories based on single-valued first-arrival traveltime tables. The imaging of a limited portion of the complex structure from a nearby reference datum allows the traveltime calculation to be performed for a restricted time range, for which the traveltime calculation accurately parameterizes the most energetic portion of the seismic wavefield. Because the first-arrival traveltime calculation is not allowed to evolve for too long, caustics and headwaves do not develop to the point where they degrade the imaging result.

1.2 Overview of the dissertation

1.2.1 Wave-equation datuming

In Chapter 2, I present a formal development of wave-equation datuming operators based on the concept of adjoint operators. I compare Kirchhoff, phase shift, and finite difference formulations both mathematically and by means of synthetic examples. In this development I present a generalized framework that links all three of the wave-equation datuming formulations. This allows me to compare their individual strengths and weaknesses, and provides an understanding of exactly how wave-equation datuming transforms data and how it differs from migration. The synthetic examples demonstrate the utility of datuming in unraveling topographic distortions and provide a practical comparison of how the different methods behave in terms of dip resolution, artifacts, and efficiency.

I conclude that Kirchhoff datuming is the best suited method for my applications because it offers the most efficient and accurate method of performing large extrapolation steps in variable velocity media. It is also readily extendible to three-dimensional applications.

1.2.2 Rugged acquisition topography

In Chapter 3, I apply the Kirchhoff datuming operator to land data to help ameliorate the effects of rugged topography. I compare the results of wave-equation datuming to statics and show that redatuming and regridding with the Kirchhoff datuming operator results in a superior stacked section and migrated image.

Seismic imaging algorithms are generally applied to data which is redatumed to a planar surface. In regions of mild topography where the near-surface velocity is much slower than the subsurface velocity, a static shift is adequate for the transformation. However, when the necessary shift increases in magnitude and when the near surface velocity is comparable to the subsurface velocity, the static approximation becomes inadequate. Under these circumstances, a static shift distorts the wavefield and degrades the velocity analysis and imaging. In this case it is necessary to propagate the wavefield numerically to some level datum. This wave-equation datuming process may be used to "flood" the topography by filling it with a replacement velocity and upward continuing the data through it.

Unlike redatuming with static shifts, wave-equation redatuming removes the distortions caused by topography in a manner consistent with wavefield propagation. This insures that subsequent processing steps which assume hyperbolic form, or even more complicated trajectories consistent with wave propagation, can be accurately applied.

For example, Figure 1.1 shows a shot gather from the Canadian foothills before and after wave-equation datuming. After wave-equation datuming the distorting effects of the topography are removed and the reflection events have laterally continuous trajectories consistent with wave propagation. The datuming operation also serves to regrid the data onto a uniformly sampled output mesh, fill in the shot gap, and attenuate steep-dip noise.

1.2.3 Layer-stripping depth migration

In Chapter 4, I describe how conventional Kirchhoff imaging with single-valued first arrivals breaks down in complex velocity models, and more importantly, I present a method of surmounting the problem. I combine Kirchhoff datuming with prestack Kirchhoff depth migration in an efficient layer-stripping depth migration algorithm and show how this approach yields excellent images in a realistic velocity model with extreme lateral velocity variations. The method is fairly robust even when the exact velocity model is not known,

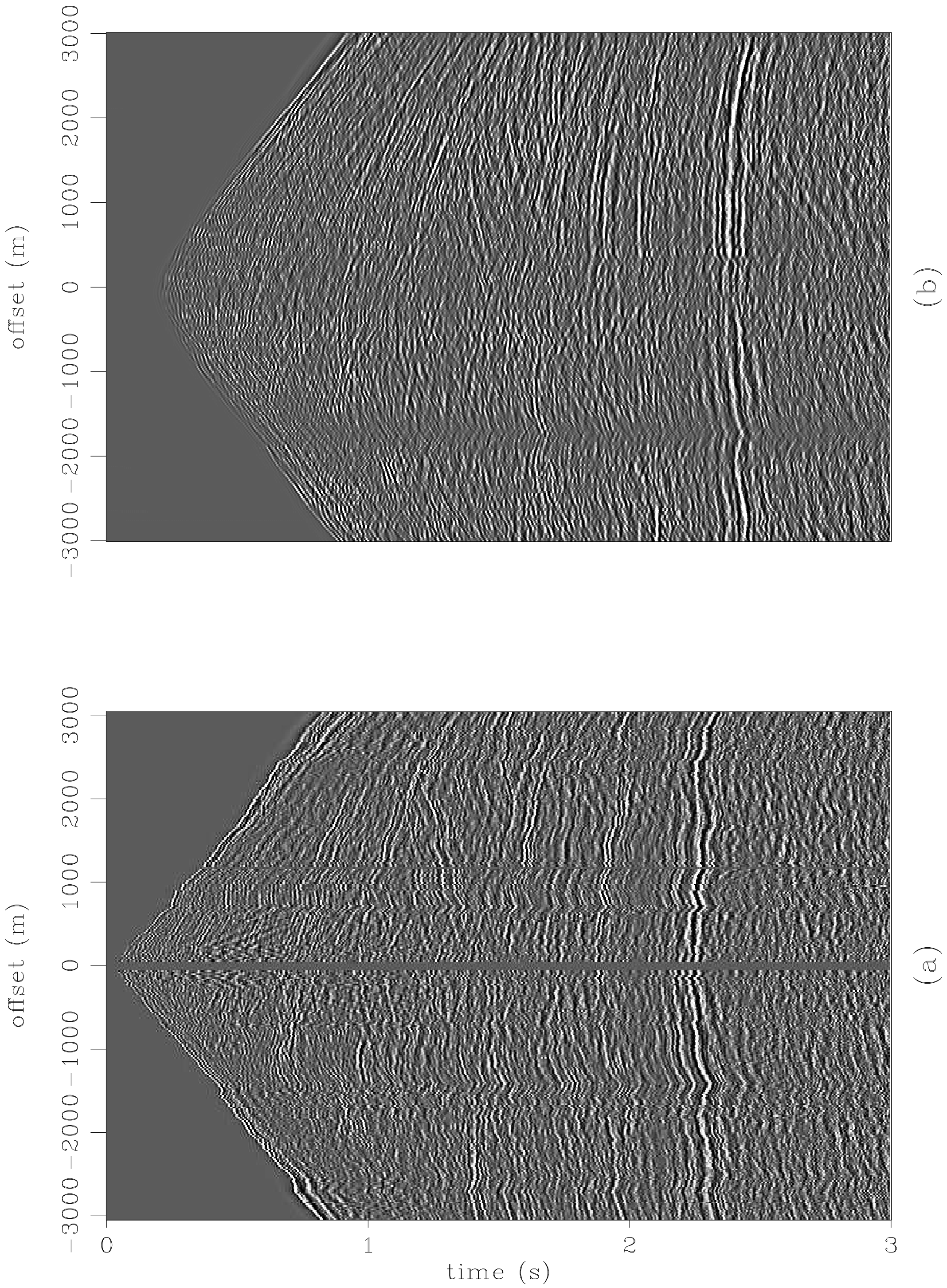

FIG. 1.1. (a) A shot gather from the Canadian foothills showing statics from rugged topography and near-surface effects. (b) Upward continuation with wave-equation datuming removes the distortions due to topography and fills in the shot gap. Movie. Intro-regsup.55 [NR]

and it produces a better image than standard Kirchhoff implementations using most energetic traveltimes and band-limited traveltimes.

The method alternates steps of datuming and imaging. Because traveltimes are computed for each step, the adverse effects of caustics and headwaves do not develop. The method is semi-recursive because the wavefield is downward continued and re-synthesized at multiple depth levels. When the imaging problem is divided in this way, the traveltimes are better behaved and some multiple arrivals are accounted for.

The great appeal of this approach is that it combines the efficiency of first-arrival Kirchhoff imaging with excellent image quality. In principle, this method only requires the same number of traveltime calculations as a standard migration. The Kirchhoff datuming steps can be implemented so that they are much more efficient than Kirchhoff migration. Therefore, the total cost of the algorithm is only a few times more than that of standard first-arrival Kirchhoff migration.

The Marmousi synthetic data set has been a popular testbed for seismic velocity estimation and imaging algorithms and it has been demonstrated that Kirchhoff algorithms using first arrival traveltimes fail even when the correct velocity model is used. This failure is illustrated in the top panel of Figure 1.2. This type of failure is disappointing because Kirchhoff migration is the most popular 2-D and 3-D prestack imaging method. This failure has stimulated the development of more accurate traveltime calculation methods that aim to handle complex propagation effects. It has led to methods that perform local averages of the velocity model in order to impose a frequency dependence on the eikonal equation (Biondi, 1992; Lomax, 1992), methods that track the most energetic arrivals, and methods which calculate traveltimes in the seismic frequency band (Nichols, 1994). Some of these methods also estimate amplitude and phase. Complicated velocity models can result in multi-valued traveltime tables, so these capabilities have also been incorporated into Kirchhoff algorithms.

My approach is based on the observation that most of the adverse effects of wavefield propagation that are difficult to parameterize with first-arrival traveltimes do not occur until the wavefield has evolved for some time. By limiting the first-arrival traveltime calculation, I am able to parameterize the asymptotic Green's functions accurately. As shown in the bottom panel of Figure 1.2, this approach leads to an excellent imaging result.

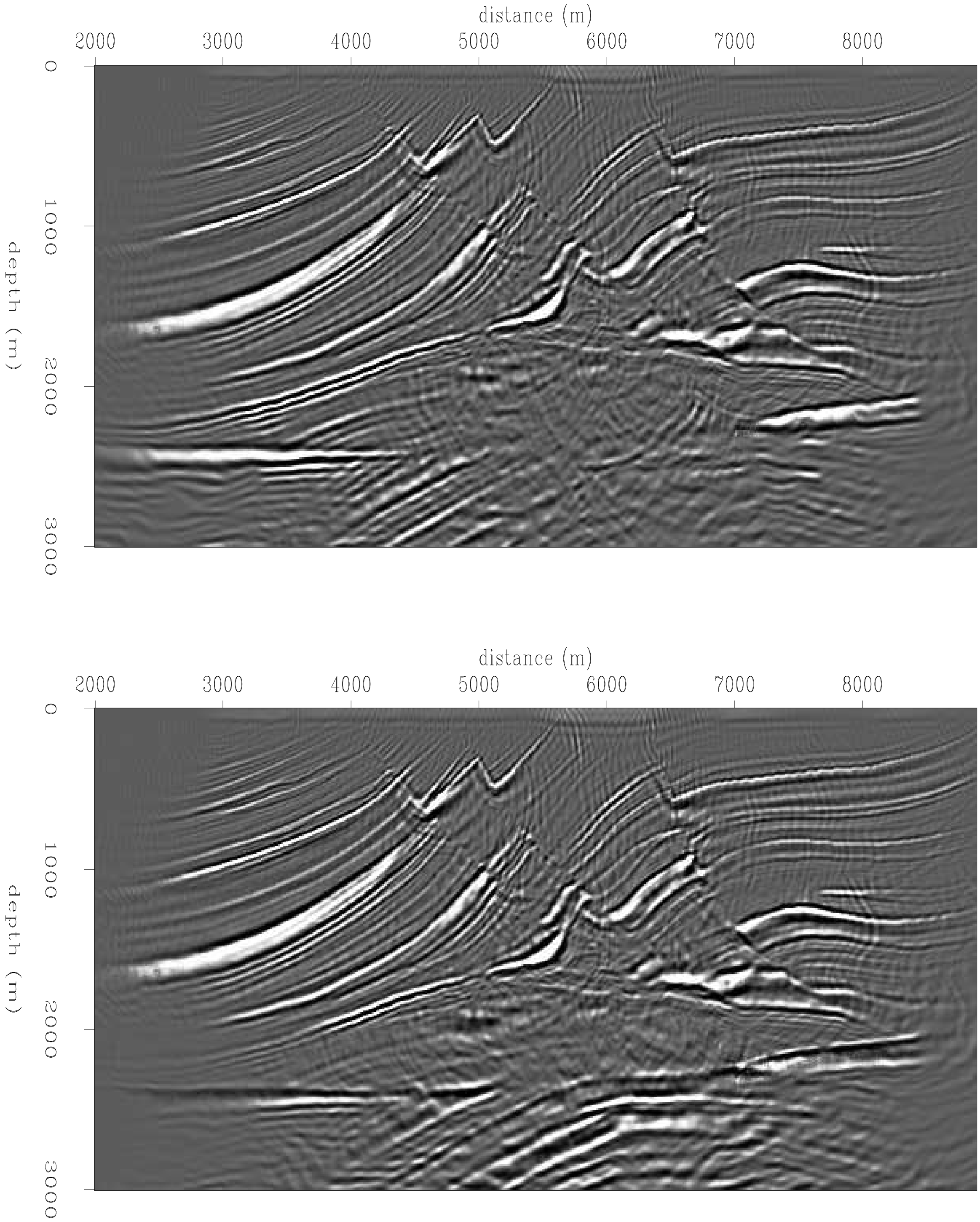

FIG. 1.2. Although standard Kirchhoff migration (top) using eikonal traveltimes produces a nice image of the upper 2000 m, it fails to image the target zone. Layer-stripping Kirchhoff migration (bottom) with eikonal traveltimes produces a nice image of the anticlinal trap structure. Movie. Intro-layerstrip [NR]

Chapter 2

Wave-equation datuming operators

Wave-equation datuming is the process of upward or downward continuing a wavefield between two arbitrarily-shaped surfaces. It is the most precise means of redatuming because it accurately implements solutions to the one-way scalar wave equation to extrapolate seismic data from the true recording surface to some arbitrary output surface. Wave-equation datuming attempts to compute the data that would have been recorded at the output surface.

The concept of wave-equation datuming was first presented by Berryhill (1979) and applied to zero-offset (poststack) data. Berryhill's method is based on an extrapolation scheme using the Kirchhoff integral solution to the scalar wave equation. Berryhill (1984) generalizes his method to prestack sections by applying the same extrapolation algorithm to common-source gathers and then to common-receiver gathers. Wiggins (1984) presents the same concept of Kirchhoff integral extrapolation of prestack data but adds an imaging step to the algorithm. With minor modification, migration algorithms based on finite-difference (Claerbout, 1985) and phase-shift (Gazdag, 1978) methods can be recast as datuming operators. Reshef (1991) presents a datuming and migration principle used in conjunction with phase-shift methods to migrate prestack data directly. He performs downward extrapolation from a flat datum and adds data to the extrapolated wavefield each time the topographic surface is intersected. Reshef's method allows direct prestack migration of data recorded on a nonflat topographic surface.

In this chapter, I formulate Kirchhoff, phase-shift, and finite-difference datuming operators using the the principle of adjoint operators. The forward problem is defined as upward continuation and the adjoint process as downward continuation. To point out the similarities and differences of the implementations, I unify the datuming concepts by presenting a matrix formulation where the forward problem is defined as a one-way wave-equation extrapolation from an irregular surface to a flat surface. This formulation is derived in a general context so that any depth extrapolation technique can be used. The adjoint problem, obtained by transposing and conjugating the forward problem, transforms the data from the level surface to the irregular topographic surface.

2.1 Kirchhoff datuming

Based on Green's second identity, the integral expression for a pressure wavefield $P(\mathbf{r}, \omega)$ within a source free volume bounded by surface S is

$$P(\mathbf{r}, \omega) \;=\; \frac{-1}{4\pi} \oint_S (P \nabla G - G \nabla P) \cdot \mathbf{n} \; dS.$$

G is a Green's function satisfying the scalar wave equation, and $\mathbf{n}$ is the inward pointing normal to the bounding surface (Figure 2.1). For seismic data, the integral can be split into two parts so that $S = S_1 + S_2$ and the wavefield can be considered as arising from causal sources below S_1, which represents the data collection surface. Since seismic data are recorded for a finite time, the surface S_2 can be chosen in such a way that the contribution from this part of the integral is negligible. The choice of Green's function that vanishes on surface S_1 reduces the integral to

$$P(\mathbf{r}, \omega) \;=\; \frac{-1}{4\pi} \int_{S_1} P \frac{\partial G}{\partial n} dS_1.$$

When the undulations of the surface are small over a wavelength, the Green's function can be approximated by

$$G \;=\; \frac{e^{ikr}}{r} \;-\; \frac{e^{ikr'}}{r'},$$

where $k = \omega / v$ and $r = ((x - x_s)^2 + (y - y_s)^2 + (z - z_s)^2)^{\frac{1}{2}}$. The subscript s indicates that the coordinate is on surface S_1. ω is angular frequency and v is propagation velocity.

FIG. 2.1. Geometry for derivation of the Kirchhoff integral (after Berkhout, 1982). Operator-greensthm [NR]

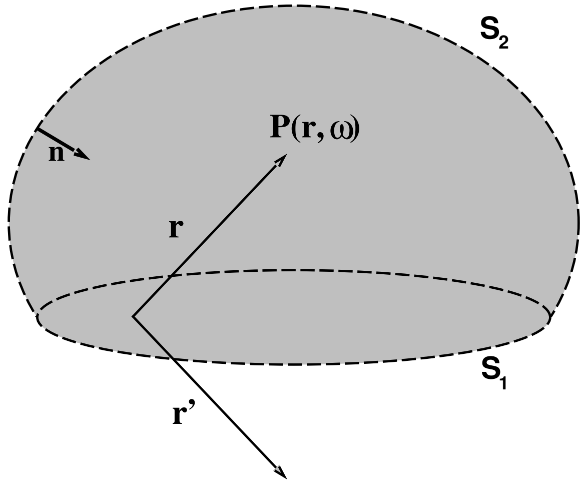

The surface integral then becomes

$$\begin{aligned} P(\mathbf{r},\omega) &= \tfrac{-1}{4\pi} \int_{S_1} P(\mathbf{r_s},\omega) \left[\tfrac{\partial}{\partial n} \tfrac{e^{ikr}}{r} - \tfrac{\partial}{\partial n} \tfrac{e^{ikr'}}{r'} \right] dS_1 \\ &= \tfrac{-1}{2\pi} \int_{S_1} P(\mathbf{r_s},\omega) \;\; \tfrac{\partial r}{\partial n} \tfrac{\partial}{\partial r} \tfrac{e^{ikr}}{r} \; dS_1 \\ &= \tfrac{1}{2\pi} \int_{S_1} P(\mathbf{r_s},\omega) \;\; \tfrac{\partial r}{\partial n} \tfrac{1-ikr}{r^2} \, e^{ikr} \; dS_1 . \end{aligned}$$

The integral can be split into near-field and far-field contributions by writing

$$P(\mathbf{r},\omega) \;=\; \frac{1}{2\pi} \int_{S_1} \frac{\partial r}{\partial n} \left[\frac{-i\omega}{rv} \, P(\mathbf{r_s},\omega) e^{i\omega\tau} + \frac{1}{r^2} \, P(\mathbf{r_s},\omega) e^{i\omega\tau} \right] dS_1, \qquad (2.1)$$

where $\tau = r/v$ represents the traveltime from the surface S_1 to the observation point $\mathbf{r}$. This equation can be recast in the time domain by using the relationships

$$\begin{aligned} -i\omega \, P(\omega) &\iff \tfrac{\partial}{\partial t} P(t), \\ P(\omega) e^{i\omega\tau} &\iff P(t-\tau), \end{aligned}$$

to obtain

$$P(\mathbf{r},t) \;=\; \frac{1}{2\pi} \int_{S_1} \frac{\partial r}{\partial n} \left[\frac{1}{rv} \frac{\partial}{\partial t} P(\mathbf{r_s}, t-\tau) + \frac{1}{r^2} P(\mathbf{r_s}, t-\tau) \right] dS_1. \qquad (2.2)$$

Equations (2.1) and (2.2) are the 3-D frequency and time domain equations for the upward continuation of a scalar wavefield. For computational efficiency it is common to make the far-field approximation $\omega/rv \gg 1/r^2$, and to drop the second term in the equations.

If the wavefield is invariant in one space coordinate, the frequency domain equation can be rewritten as

$$P(\mathbf{r},\omega) \;=\; \frac{1}{2\pi}\int_x P(\mathbf{r_S},\omega)\int_y \frac{\partial r}{\partial n}\,\frac{1-ikr}{r^2}\,e^{ikr}\,dy\,dx.$$

Integrating out the y dependence by the method of stationary phase yields

$$P(\mathbf{r},\omega) \;=\; \frac{1}{v\sqrt{2\pi}}\int_x \frac{\partial r}{\partial n}\left[\frac{\sqrt{-i\omega}}{\sqrt{t}} \;+\; \frac{1}{t^{3/2}\sqrt{-i\omega}}\right] P(\mathbf{r_S},\omega)\,e^{i\omega t}\,dx. \tag{2.3}$$

Making the far-field approximation yields

$$P(\mathbf{r},\omega) \;=\; \frac{1}{\sqrt{2\pi v}}\int_x \frac{\partial r}{\partial n}\,\sqrt{-i\omega}\,P(\mathbf{r_S},\omega)\,\frac{e^{i\omega\tau}}{\sqrt{r}}\,dx. \tag{2.4}$$

The equivalent time domain expression is

$$P(\mathbf{r},t) \;=\; \frac{1}{\sqrt{2\pi v}}\int_x \frac{\partial r}{\partial n}\,\frac{1}{\sqrt{r}}\,D_{\frac{1}{2}} * P(\mathbf{r_S},t-\tau)\,dx. \tag{2.5}$$

For the 2-D versions of the integrals, $r = ((x-x_s)^2 + (z-z_s)^2)^{\frac{1}{2}}$. The term $D_{\frac{1}{2}}$ is a convolutional operator corresponding to frequency domain multiplication by $\sqrt{-i\omega}$. Rather than making the far-field approximation, Berryhill (1979) obtains a 2-D version in the time domain by integrating out the y dependence of equation (2.2). His expression is similar to equation (2.5), except that his convolutional operator depends on r. Berryhill's time domain formulation is accurate since it includes the near-field term, but in practice, the added computation of the delay-time variant convolution is often unnecessary.

Equations (2.1) through (2.5) are the Kirchhoff integral equations for upward continuation. Wave-equation datuming is performed by implementing these equations. Downward continuation is performed by means of the adjoint processes. The concept of adjoint operators will be more fully described in a subsequent section, but for now, it is only important to note that the adjoint forms of the integral equations will have the opposite sign in $i\omega$ or in the time delay factor $\tau = r/v$. The adjoint forms of the time domain integrals, along with the imaging condition, result in Schneider's (1978) Kirchhoff migration operators. Wiggins (1984) uses the far-field approximation in his implementation of Kirchhoff datuming and migration.

2.1.1 Discrete matrix formulation of Kirchhoff datuming

For transformation of a wavefield from one datum to another, as depicted in Figure 2.2, a discrete form of equation (2.4) is

$$P_j(\omega) \;=\; \sum_i A_{ij}\,\sqrt{-i\omega}\,P_i(\omega)e^{i\omega\tau_{ij}}. \tag{2.6}$$

A_{ij} is an amplitude term incorporating divergence and obliquity, and τ_{ij} is the traveltime between input location i and output location j. The equivalent time domain equation is

$$P_j(t) \;=\; \sum_i A_{ij}\,D_{\frac{1}{2}} * P_i(t-\tau_{ij}). \tag{2.7}$$

If the far-field approximation were not invoked, the $D_{\frac{1}{2}}$ operator would be replaced by an i,j-variable convolution operator. The 3-D equations are algorithmically identical, except that the half-order derivative is replaced by a full derivative, and the amplitude terms

$$A_{ij} \;=\; \frac{\Delta x}{\sqrt{2\pi r_{ij} v}}\cos\theta_{ij},$$

are replaced by

$$A_{ij} \;=\; \frac{\Delta x\,\Delta y}{2\pi r_{ij} v}\cos\theta_{ij}.$$

θ_{ij} is the angle between the normal to the input surface and the traveltime path connecting input location i and output location j. The $\cos\theta_{ij}$ factor arises from the identity

$$\frac{\partial r}{\partial n} \;=\; \nabla r\cdot\mathbf{n}.$$

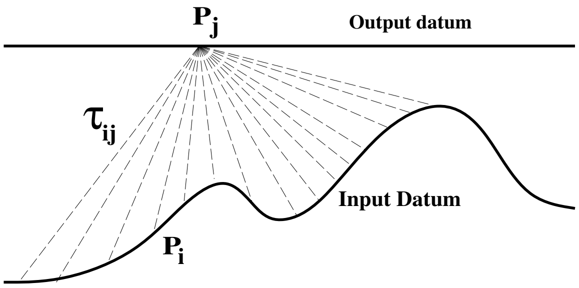

FIG. 2.2. Schematic representation of Kirchhoff upward continuation corresponding to implementation of equation (2.6) or equation (2.7). Each input trace P_i is filtered, time shifted according to τ_{ij}, scaled, and summed into output trace P_j. $\boxed{\text{Operator-kwed}}$ [NR]

For the special illustrative case of three input traces, equation (2.6) can be expressed in matrix form as

$$[P(x_j,z_j,\omega)] \;=\; \begin{bmatrix} I & I & I \end{bmatrix} \begin{bmatrix} Z_{11} & & \\ & Z_{12} & \\ & & Z_{13} \end{bmatrix} \begin{bmatrix} H & & \\ & H & \\ & & H \end{bmatrix} \begin{bmatrix} P(x_{i=1},z_{i=1},\omega) \\ P(x_{i=2},z_{i=2},\omega) \\ P(x_{i=3},z_{i=3},\omega) \end{bmatrix},$$

where $P(x_i, z_i, \omega)$ is the Fourier-transformed input wavefield recorded at datum z_i and $P(x_j, z_j, \omega)$ is an output trace at location (x_j, z_j). A half-order derivative is applied to the input data by the block matrices

$$H = \begin{bmatrix} \sqrt{-i\omega_1} & & & & & \\ & \sqrt{-i\omega_2} & & & & \\ & & \cdot & & & \\ & & & \cdot & & \\ & & & & \cdot & \\ & & & & & \sqrt{-i\omega_n} \end{bmatrix}.$$

The block matrices Z_{11}, Z_{12}, and Z_{13} perform time shifts and amplitude scaling of individual data traces. For a given time shift τ_{ij}, the time-shift matrix is given by

$$Z_{ij} = \begin{bmatrix} A_{ij}e^{i\omega_1\tau_{ij}} & & & & & \\ & A_{ij}e^{i\omega_2\tau_{ij}} & & & & \\ & & \cdot & & & \\ & & & \cdot & & \\ & & & & \cdot & \\ & & & & & A_{ij}e^{i\omega_n\tau_{ij}} \end{bmatrix}. \tag{2.8}$$

The A_{ij} factors are amplitude scaling terms which embody the effects of spherical divergence and obliquity. Finally, the summation of the shifted input traces is represented by matrix multiplication with the row vector having block identity matrices I as its elements. The summation matrix and the Z_{ij} matrix can be combined to simplify the matrix equation to

$$[P(x_j, z_j, \omega)] = \begin{bmatrix} Z_{11} & Z_{12} & Z_{13} \end{bmatrix} \begin{bmatrix} H & & \\ & H & \\ & & H \end{bmatrix} \begin{bmatrix} P(x_{i=1}, z_{i=1}, \omega) \\ P(x_{i=2}, z_{i=2}, \omega) \\ P(x_{i=3}, z_{i=3}, \omega) \end{bmatrix}. \tag{2.9}$$

Equation (2.9) can be generalized to multiple output traces. For illustrative purposes, I write down the matrix equation for three input traces and three output traces. The wavefield at the upper datum is

$$\begin{bmatrix} P(x_{j=1}, z_{j=1}, \omega) \\ P(x_{j=2}, z_{j=2}, \omega) \\ P(x_{j=3}, z_{j=3}, \omega) \end{bmatrix} = \begin{bmatrix} Z_{11} & Z_{12} & Z_{13} \\ Z_{21} & Z_{22} & Z_{23} \\ Z_{31} & Z_{32} & Z_{33} \end{bmatrix} \begin{bmatrix} H & & \\ & H & \\ & & H \end{bmatrix} \begin{bmatrix} P(x_{i=1}, z_{i=1}, \omega) \\ P(x_{i=2}, z_{i=2}, \omega) \\ P(x_{i=3}, z_{i=3}, \omega) \end{bmatrix}. \tag{2.10}$$

The time-shift matrices Z_{ij} correspond to equation (2.8) with ij corresponding to the time shift τ_{ij} between input and output locations i and j. In actual implementation, more than three traces are required for summation to represent integration adequately. Three traces are used here merely for ease of exposition, and to establish a pattern which is trivial to extend to more traces.

Equation (2.10) represents the upward continuation of a wavefield between two arbitrarily-shaped surfaces. The downward continuation operator is derived by taking the complex conjugate transpose of the operator in equation (2.10). This yields the adjoint operator:

$$\begin{bmatrix} H^* & & \\ & H^* & \\ & & H^* \end{bmatrix} \begin{bmatrix} Z_{11}^* & Z_{21}^* & Z_{31}^* \\ Z_{12}^* & Z_{22}^* & Z_{32}^* \\ Z_{13}^* & Z_{23}^* & Z_{33}^* \end{bmatrix}. \tag{2.11}$$

Equation (2.11) is the downward continuation operator which is depicted in Figure 2.3 for one output trace.

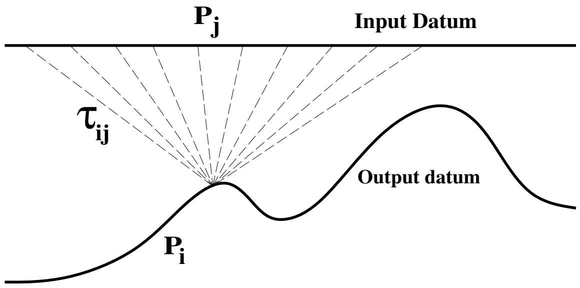

FIG. 2.3. Schematic representation of Kirchhoff downward continuation corresponding to the operator of equation (2.11). Each input trace P_j is filtered, time shifted according to τ_{ij}, scaled, and summed into output trace P_i. Operator-kweddown [NR]

These matrix representations result in huge, albeit sparse, operator matrices. In the actual computer implementation of Kirchhoff datuming these huge matrix operators are not actually stored. The numerical algorithms apply these linear operators indirectly and much more efficiently.

In order to understand why Kirchhoff datuming is much more efficient than Kirchhoff time migration, it is instructive to look at the kinematics of the two processes. Kirchhoff datuming is performed by summing along a trajectory given by

$$t_{\text{datum}} = t_{\text{obs}} + \sqrt{\frac{z_{\text{datum}}^2}{v^2} + \frac{x^2}{v^2}}.$$

This is the equation of a time-shifted hyperbola. The variable z_{datum} is the vertical datuming distance, which remains fixed, so each input trace is shifted by a time-invariant amount. This is illustrated in Figure 2.4a for the simple case of extrapolation between two level datums. Time migration is performed by invoking the imaging condition (setting $t_{\rm obs} = 0$) and performing the summation for each image point $t_0 = z_{\rm depth}/v$. The resulting summation trajectory is given by

$$t_{\rm mig} = \sqrt{t_0^2 + \frac{x^2}{v^2}}.$$

The traces are shifted by a time-variant amount because t_0 changes with depth for every image point. This is illustrated in Figure 2.4b.

Most of the Kirchhoff datuming results in this dissertation are generated by implementing equation (2.6) on Thinking Machine's massively parallel CM5 (Bevc, 1993). The frequency domain is computationally attractive because the static time shift and the convolutional filtering are both efficiently applied by complex multiplication. This frequency domain implementation makes Kirchhoff datuming much more efficient than time domain Kirchhoff migration.

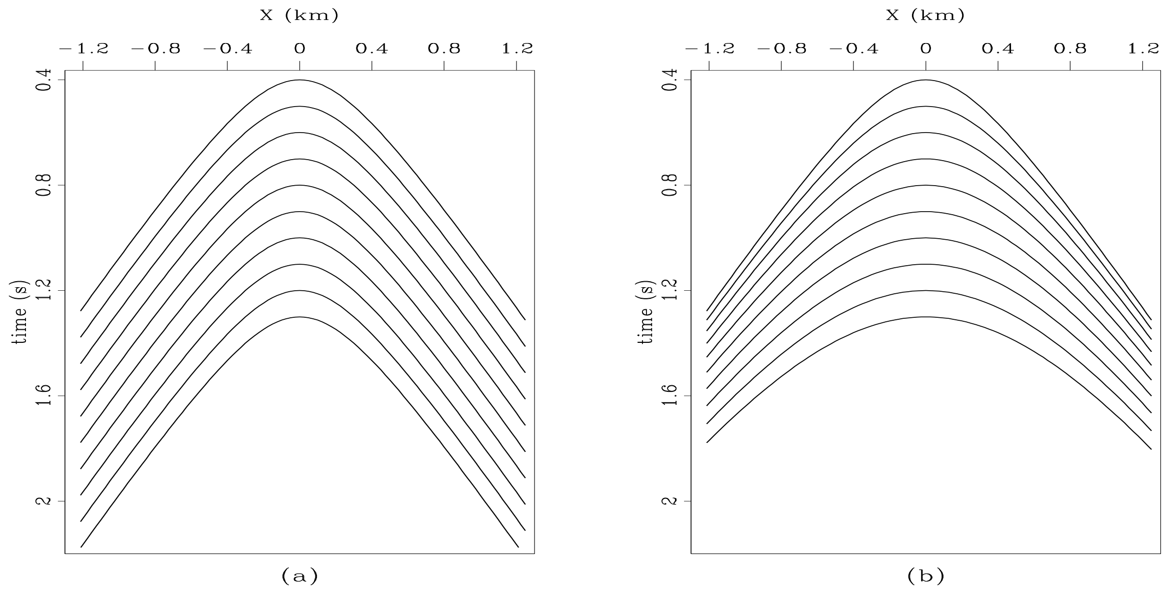

FIG. 2.4. Comparison of (a) datuming and (b) migration summation trajectories. Datuming is much less computationally intensive because each trace is shifted by a time-invariant amount. Operator-trajectory [R]

Prestack datuming is performed by using reciprocity to extrapolate shot and receiver gathers (Berryhill, 1984). This can be represented mathematically by the double summation

$$P(\mathbf{r}_s, \mathbf{r}_g, t) \ = \ \sum_{\xi_s} \sum_{\xi_g} A(\mathbf{r}_s, \xi_s) A(\mathbf{r}_g, \xi_g)\, D * P(\xi_s, \xi_g, t - \tau(\mathbf{r}_s, \xi_s) - \tau(\mathbf{r}_g, \xi_g)). \qquad (2.12)$$

This corresponds to a discrete form of Wiggin's KRK integral (1984). In this representation, the original data are recorded on surface S_1 with surface coordinates (ξ_s, ξ_g). The summations over ξ_s and ξ_g represent integration over the shot and receiver coordinates. $A(\mathbf{r}_*, \xi_*)$ and $\tau(\mathbf{r}_*, \xi_*)$ represent amplitude and traveltime delay in either shot $(* = s)$ or receiver $(* = g)$ gathers. Because both shot and group gathers are datumed, for 2-D the convolutional operator $D = D_{\frac{1}{2}} * D_{\frac{1}{2}}$ corresponds to filtering with a full derivative operator, and for 3-D data D corresponds to filtering with a second-order derivative operator. This sum is performed for all output shot $\mathbf{r}_s$ and receiver $\mathbf{r}_g$ coordinates.

So far, this development has been for constant velocity media. In variable velocity media, the calculation of the Green's functions becomes more complicated. The most common way of handling complex velocity structure with Kirchhoff methods is by calculating the traveltime shift τ using ray tracing or finite-difference solutions to the eikonal equation. I choose to use eikonal traveltimes calculated with van Trier and Symes' (1991) upwind finite-difference algorithm. In Chapter 4 I demonstrate that this gives excellent results, even for complex velocity models such as the Marmousi synthetic.

2.2 Phase-shift datuming

The 3-D Kirchhoff integral (equation (2.2)) can be written as a convolution which, as shown by Schneider (1978), can be Fourier transformed over x, y, and t coordinates so that it becomes complex multiplication in the frequency-wavenumber domain:

$$P(k_x, k_y, z, \omega) \ = \ P(k_x, k_y, z_0, \omega) \cdot e^{i k_z \Delta z}. \qquad (2.13)$$

The term k_z embodies the dispersion relationship, and is given by

$$k_z \ = \ \sqrt{\frac{\omega^2}{v^2} - k_x^2 - k_y^2}.$$

The choice of sign in the exponent determines the direction of extrapolation. The corresponding 2-D equations are obtained by setting $k_y = 0$.

For a constant value of k_z, equation (2.13) is the analytic solution to the ordinary differential equation,

$$\frac{\partial^2 P(k_x, k_y, z, \omega)}{\partial(\Delta z)^2} + k_z^2 P(k_x, k_y, z, \omega) \;=\; 0,$$

which forms the basis of Gazdag's (1978) phase-shift wave-extrapolation formulation. This form of the wave equation is valid for all values of ω, k_x, and k_y.

For depth variable velocity $v(z)$, k_z is considered constant for small depth intervals (Δz) where the velocity is approximately constant. Therefore, the 2-D version of equation (2.13) can be written as

$$P(k_x, z = z_0 - \Delta z, \omega) = P(k_x, z = z_0, \omega) e^{ik_z \Delta z}. \tag{2.14}$$

This form of the equation is used to downward or upward extrapolate the wavefield for small depth intervals.

The phase-shift datuming operation can be written in matrix form by concatenating a sequence of successive operator matrices. For simplicity, I consider upward continuation from a surface with three depth levels, to a flat output datum (Figure 2.5). The algorithm can be generalized for any number of depth levels and any datum geometry.

The operation of phase-shift datuming begins by picking data that corresponds to depth levels on a numerical grid. This picking can be represented by multiplication with matrices that correspond to the shape of the datum. For the case shown in Figure 2.5, these matrices are

$$A = \begin{bmatrix} 1 & & & & & \\ & 1 & & & & \\ & & . & & & \\ & & & . & & \\ & & & & . & \\ & & & & & . \end{bmatrix}, B = \begin{bmatrix} . & & & & & \\ & . & & & & \\ & & 1 & & & \\ & & & 1 & & \\ & & & & . & \\ & & & & & . \end{bmatrix}, C = \begin{bmatrix} . & & & & & \\ & . & & & & \\ & & . & & & \\ & & & . & & \\ & & & & 1 & \\ & & & & & 1 \end{bmatrix}.$$

The phase-shift extrapolation operation corresponding to equation (2.14) is represented by the matrices W_1, W_2, W_3, where

$$W_i = \begin{bmatrix} e^{ik_{zi1}\Delta z} & & & \\ & e^{ik_{zi2}\Delta z} & & \\ & & \ddots & \\ & & & e^{ik_{zi6}\Delta z} \end{bmatrix}. \tag{2.15}$$

Each diagonal contains the phase-shifting exponentials necessary to upward extrapolate the wavefield to a depth level. The value of $(k_z)_{ij}$ is given by the dispersion relation,

$$(k_z)_{ij} = \sqrt{\frac{\omega^2}{v(z_i)^2} - k_{xj}^2}.$$

Referring to Figure 2.5, upward continuation of the wavefield $P = P(x, z_s, \omega)$ can be implemented in the following sequence of steps:

1. The traces from level A are upward continued to level B by

$$F^* W_1 F A P,$$

F represents the Fourier transform of the horizontal space variable and F^* represents the inverse Fourier transform of the horizontal space variable.

2. The traces from level B, plus the traces from the previous step, are upward continued to level C by

$$F^* W_2 F[F^* W_1 F A P + BP].$$

3. Finally, the traces from level C , plus the traces from the previous step, are upward continued to the flat output datum:

$$F^* W_3 F[[F^* W_2 F[F^* W_1 F A P + BP]] + CP].$$

So, for each value of ω, the output wavefield $P(x, z_{\mathrm{dat}}, \omega)$ is given by

$$\begin{bmatrix} F^* \end{bmatrix} \begin{bmatrix} W_3 W_2 W_1 & W_3 W_2 & W_3 \end{bmatrix} \begin{bmatrix} F & & \\ & F & \\ & & F \end{bmatrix} \begin{bmatrix} A \\ B \\ C \end{bmatrix} \begin{bmatrix} P(x, z_s, \omega) \end{bmatrix}. \qquad (2.16)$$

where $P(x, z_s, \omega)$ is a column vector representing the wavefield recorded on the topographic datum.

The adjoint algorithm can be obtained by reversing the order of matrix multiplication in equation (2.16) and transposing and conjugating each matrix. The matrices A, B, C, are diagonal matrices and therefore equal to their transpose. For each value of the frequency ω, the adjoint datuming operator is

$$\begin{bmatrix} A & B & C \end{bmatrix} \begin{bmatrix} F^* & & \\ & F^* & \\ & & F^* \end{bmatrix} \begin{bmatrix} W_1^* W_2^* W_3^* \\ W_2^* W_3^* \\ W_3^* \end{bmatrix} \begin{bmatrix} F \end{bmatrix}. \qquad (2.17)$$

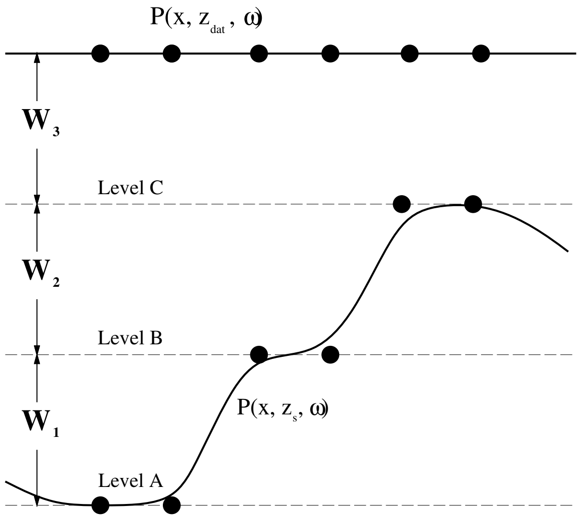

FIG. 2.5. Schematic representation of phase-shift upward continuation corresponding to implementation of equation (2.16). The data are extrapolated from level A by matrix W_1, from level B by matrix W_2, and from level C by matrix W_3. Operator-gazwed [NR]

The matrices W_i^* are the adjoints of the diagonal matrices W_i, which are explicitly represented in equation (2.15).

The matrix formulation presented here is similar to that developed by Popovici (1992) and by Ji and Claerbout (1992), except that their forward operators take data from a flat surface and upward continued to an irregular datum. Their formulations are more closely aligned with Reshef's (1991) algorithm for migration from irregular surfaces. In fact, Popovici's and Ji and Claerbout's forward operators are necessarily the adjoint of Reshef's downward continuation operator.

Regardless of how these methods are formulated, the underlying principle is the same. A computational grid is laid out, and the extrapolation begins either above or below the topography, the data are inserted into the extrapolation as the wavefield passes the grid points which coincide with the topography.

Prestack datuming can be performed as described for the Kirchhoff method by extrapolating shot and receiver gathers separately. However, since the phase-shift operator is applied recursively for each Δz interval, prestack datuming can also be performed by definition of shot and receiver wavenumbers and implementation of equation (2.14) so that shot gathers and receiver gathers are upward continued separately over each Δz interval. This is the adjoint of the double square root (DSR) operator (Yilmaz and Claerbout, 1980).

2.2.1 Phase-shift datuming with lateral velocity variation

For laterally-variant media, phase-shift datuming can be performed by using an adaptation of Gazdag and Sguazzero's (1984) phase shift plus interpolation (PSPI) method. In this method, the wavefield is extrapolated at multiple velocities and a single upward-propagated wavefield is obtained by interpolation. Linear interpolation of two wavefields P_1 and P_2 is an operation of the type

$$\begin{bmatrix} \tilde{P} \end{bmatrix} = \begin{bmatrix} w_1 & w_2 \end{bmatrix} \begin{bmatrix} P_1 \\ P_2 \end{bmatrix},$$

where the adjoint operator spreads a value with two weights w_1 and w_2:

$$\begin{bmatrix} \tilde{P}_1 \\ \tilde{P}_2 \end{bmatrix} = \begin{bmatrix} w_1 \\ w_2 \end{bmatrix} \begin{bmatrix} P \end{bmatrix}.$$

The PSPI upward datuming operator for the geometry of Figure 2.5 can be written as

$$\begin{bmatrix} U_3 U_2 U_1 & U_3 U_2 & U_3 \end{bmatrix} \begin{bmatrix} A \\ B \\ C \end{bmatrix} \begin{bmatrix} P(x, z_s, \omega) \end{bmatrix}, \tag{2.18}$$

where the matrices U_i represent the extrapolation operators for laterally-variant velocity. The matrix U_i can be further decomposed into the sequence

$$\begin{bmatrix} w_1 & w_2 \end{bmatrix} \begin{bmatrix} F^* & \\ & F^* \end{bmatrix} \begin{bmatrix} W_{i1} & \\ & W_{i2} \end{bmatrix} \begin{bmatrix} I \\ I \end{bmatrix} \begin{bmatrix} F \end{bmatrix}. \tag{2.19}$$

The physical interpretation of equation (2.19) is that the wavefield, after Fourier transformation, is split and upward continued with two different velocities. The two wavefields are independently inverse Fourier transformed and then interpolated. This sequence is repeated for each depth level.

The adjoint algorithm is found by transposing each matrix and reversing the multiplication order, as follows:

$$\begin{bmatrix} A & B & C \end{bmatrix} \begin{bmatrix} U_1^* U_2^* U_3^* \\ U_2^* U_3^* \\ U_3^* \end{bmatrix} \begin{bmatrix} P(x, z_{\mathrm{dat}}, \omega) \end{bmatrix}. \tag{2.20}$$

The matrices U_i^* represent the operator for downward continuation of the wavefield to the depth level i. The matrix U_i^* is obtained by taking the adjoint of equation (2.19):

$$\begin{bmatrix} F^* \end{bmatrix} \begin{bmatrix} I & I \end{bmatrix} \begin{bmatrix} W_{i1}^* & \\ & W_{i2}^* \end{bmatrix} \begin{bmatrix} F & \\ & F \end{bmatrix} \begin{bmatrix} w_1 \\ w_2 \end{bmatrix}. \qquad (2.21)$$

Popovici (1992) shows that the Split-Step formulation is similar, and that the only difference is in the U_i matrices.

2.3 Finite-difference datuming

Finite-difference wave extrapolation is performed by transforming the dispersion relation into a differential equation (Claerbout, 1985). In 2-D, the dispersion relationship

$$k_z = \frac{\omega}{v}\sqrt{1 - \frac{v^2 k_x^2}{\omega^2}},$$

is converted to a differential equation by substituting $ik_z \rightarrow \partial/\partial z$, to get

$$\frac{\partial P}{\partial z} = \frac{i\omega}{v}\sqrt{1 - \frac{v^2}{\omega^2}k_x^2}\, P.$$

Muir's continued fraction expansion approximation to the square root and the substitution $ik_x \rightarrow \partial/\partial x$ yields the 15° equation

$$\frac{\partial P}{\partial z} = \frac{i\omega}{v(x,z)} P + \frac{v(x,z)}{-i2\omega}\frac{\partial^2 P}{\partial x^2}. \qquad (2.22)$$

Depth stepping proceeds by solution of equation (2.22) in two stages. The first stage,

$$\frac{\partial P}{\partial z} = \frac{i\omega}{v} P,$$

is solved analytically by

$$P(z - \Delta z) = P(z) e^{\frac{i\omega}{v}\Delta z}.$$

The second stage,

$$\frac{\partial P}{\partial z} = \frac{v}{-i2\omega}\frac{\partial^2 P}{\partial x^2},$$

is solved by use of some method of finite differencing. For a given depth step, Δz, the finite-difference extrapolation is given by the product $D_i L_i$, where D_i is a matrix representation of the finite-difference solution method. In principle this could be any solver, but in practice the examples in this dissertation are solved using the Crank-Nicholson implicit method (Claerbout, 1985).

For the geometry of Figure 2.5, L_i is the matrix

$$\begin{bmatrix} e^{i\frac{\omega}{v(x_1,z_i)}\Delta z} & & & \\ & e^{i\frac{\omega}{v(x_2,z_i)}\Delta z} & & \\ & & \ddots & \\ & & & e^{i\frac{\omega}{v(x_6,z_i)}\Delta z} \end{bmatrix}.$$

Therefore, the upward continuation operator can be written as

$$\begin{bmatrix} D_3L_3D_2L_2D_1L_1 & D_3L_3D_2L_2 & D_3L_3 \end{bmatrix} \begin{bmatrix} A \\ B \\ C \end{bmatrix} \begin{bmatrix} P(x, z_s, \omega) \end{bmatrix}, \tag{2.23}$$

The adjoint algorithm is found by transposing each matrix and reversing the multiplication order, as follows:

$$\begin{bmatrix} A & B & C \end{bmatrix} \begin{bmatrix} L_1^*D_1^*L_2^*D_2^*L_3^*D_3^* \\ L_2^*D_2^*L_3^*D_3^* \\ L_3^*D_3^* \end{bmatrix} \begin{bmatrix} P(x, z_{\text{dat}}, \omega) \end{bmatrix}. \tag{2.24}$$

Prestack finite-difference datuming can be performed by extrapolation of shot and receiver gathers separately or by implementation of the double square root equation,

$$\frac{\partial P}{\partial z} = \left[\sqrt{\left(\frac{i\omega}{v(x_g)}\right)^2 + \frac{\partial^2}{\partial x_g^2}} + \sqrt{\left(\frac{i\omega}{v(x_s)}\right)^2 + \frac{\partial^2}{\partial x_s^2}} \right] P(x_s, x_g, \omega),$$

and alternation between shot x_s and group x_g coordinates for every depth step Δz.

2.4 Generalized formulation of wave-equation datuming

I can unify the datuming formulations of the previous sections by observing that they can all be cast in the same general framework. Suppose that a wavefield is recorded on an irregular datum. The forward problem is to upward continue the wavefield to some flat surface, as schematically represented in Figure 2.5. The algorithm begins by upward continuing the data from the lowest point on the topographic datum. Each time the wavefield reaches a point where the computational grid coincides with the datum, data are inserted into the upward-propagated wavefield. The adjoint process starts by downward continuing the data from a flat surface, and each time the computation reaches the irregular datum, the values of the wavefield are extracted at the appropriate location.

The wavefield can be propagated upward using any wave-equation depth extrapolation technique (Kirchhoff, phase-shift, or finite-difference) discussed in the previous sections. The generalized form of the upward continuation datuming operator corresponding to the geometry of Figure 2.5 can be written as

$$\begin{bmatrix} P(x, z_{\text{dat}}, \omega) \end{bmatrix} = \begin{bmatrix} W_3 W_2 W_1 & W_3 W_2 & W_3 \end{bmatrix} \begin{bmatrix} A \\ B \\ C \end{bmatrix} \begin{bmatrix} P(x, z_s, \omega) \end{bmatrix}. \tag{2.25}$$

The propagator matrices, W_i, can represent:

- Finite-difference extrapolation. In this case, W_i corresponds to the operator $D_i L_i$ in equation (2.23).

- Phase-shift extrapolation. For $v(z)$, W_i corresponds to the operator $F^* W_i F$ in equation (2.16). For $v(x, z)$, W_i corresponds to the PSPI operator U_i defined in equation (2.19).

- Kirchhoff extrapolation. For Kirchhoff extrapolation, each W_i represents an application of equation (2.10) between level datums. Since this generalized formulation of datuming uses smaller depth steps than are commonly used with Kirchhoff methods, it is critical that the near-field term of equation (2.1) or equation (2.2) is retained.

The downward continuation datuming operator is given by the adjoint of equation (2.25):

$$\begin{bmatrix} \tilde{P}(x, z_s, \omega) \end{bmatrix} = \begin{bmatrix} A & B & C \end{bmatrix} \begin{bmatrix} W_1^* W_2^* W_3^* \\ W_2^* W_3^* \\ W_3^* \end{bmatrix} \begin{bmatrix} P(x, z_{\text{dat}}, \omega) \end{bmatrix}, \tag{2.26}$$

where W_i are the corresponding adjoint extrapolation operators.

2.5 Synthetic examples

In this section I apply the Kirchhoff, phase-shift, and finite-difference wave-equation datuming operators to synthetic data in order to compare them and to demonstrate some basic characteristics of the datuming process. To gain the full benefit of wave-equation datuming, data should generally be datumed prestack; however, I examine the zero-offset case here because it is a first step in gaining intuition into how wave-equation datuming transforms the data and also because it is easy to visualize what the zero-offset synthetics should look like.

The subsurface model for the synthetic data consists of an anticline, a syncline, and two point diffractors in a constant velocity media. The medium velocity is 2 km/s. Topography is modeled as a 200 m high cosine shaped mountain (Figure 2.6). The result of zero-offset Kirchhoff modeling is shown in Figure 2.7a. The effect of the topography is the creation of a low frequency undulation which completely distorts the synthetic data.

FIG. 2.6. Topography and subsurface structure used to generate the zero-offset synthetic data. The two point diffractors are depicted by astrecies above and below the anticline/syncline structure. Operator-submodel [R]

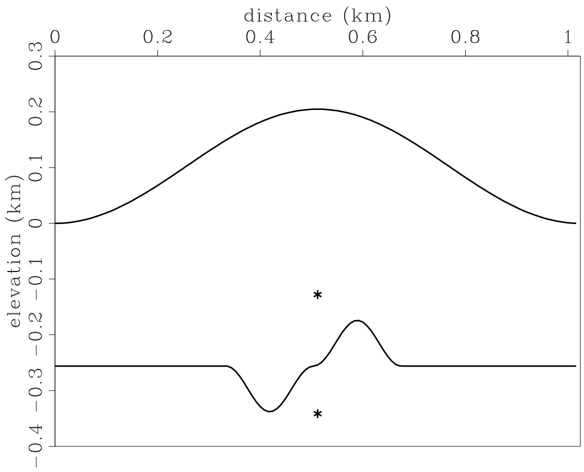

2.5.1 Upward continuation

Upward continuing the synthetic data removes the distortions. Figures 2.7b through 2.7d are the result of upward continuing the synthetic of Figure 2.7a with the Kirchhoff, finite-difference, and phase-shift operators. The output datum for all these upward continuations is just above the highest topography at a datum elevation of 210 m. The results exhibit different types of artifacts, but they are all kinematically correct. The Kirchhoff result is the most pleasing, with the fewest artifacts.

The Kirchhoff result is generated using the one-step time domain formulation of equation (2.7). In this instance, the near-field term has been retained and the $D_{\frac{1}{2}}$ operator has been replaced by a convolutional operator which depends on the delay τ. The corresponding matrix formulation is the time domain equivalent of equation (2.10) with H operator submatrices replaced by τ-dependant convolutional operators.

The finite-difference result is generated using the 45° equation and corresponds to the matrix formulation of equation (2.23). This result exhibits boundary artifacts and finite-difference dispersion. The phase-shift result is generated using an implementation corresponding to the matrix formulation of equation (2.16). It is kinematicly equivalent to the other two upward continuations, but exhibits Fourier wrap-around artifacts. The result is more aesthetically pleasing than the finite-difference result, but has more artifacts than the output of the Kirchhoff method.

The results of upward continuation can be compared with Figure 2.8, which is the result of calculating the synthetic result directly at the datum elevation of 210 m. This Figure represents the desired output of the datuming algorithms, and it is best matched by the Kirchhoff datuming result. There are minor differences between Figure 2.8 and Figure 2.7b. There is an imperceptible phase shift between the two figures, and there are a few added artifacts in the datuming result. For the most part, the Kirchhoff datuming result matches Figure 2.8 very well.

In Figure 2.9a, the synthetic data are migrated using the adjoint of the program which generated the synthetic. This migration requires knowledge of the subsurface velocity. In Figures 2.9b through 2.9c the upward continued synthetics of Figures 2.7b through 2.7c are migrated from the flat datum. These three migrations were performed with the same Kirchhoff imaging algorithm. In these migrations it is evident how the different dip components of the wavefield are transformed by the different datuming operators. The migration after finite-difference datuming results in the poorest image because of the dip limitations of the 45° approximation to the one-way wave equation. The flanks of the anticline/syncline are not imaged and the point diffractors are poorly imaged. The migration after Kirchhoff datuming (Figure 2.9b) images all the features of the subsurface model. This is because in the Kirchhoff datuming step, much of the high dip energy has been captured during the upward continuation by padding traces on either side of the section. The migration after phase-shift datuming (Figure 2.7d) results in a satisfactory image that compares favorably with the result of imaging from the topography (Figure 2.9a). The phase-shift method preserves the steep dips, and performs much better than the finite-difference method. In the phase-shift method, some of the steep dip energy is wrapped

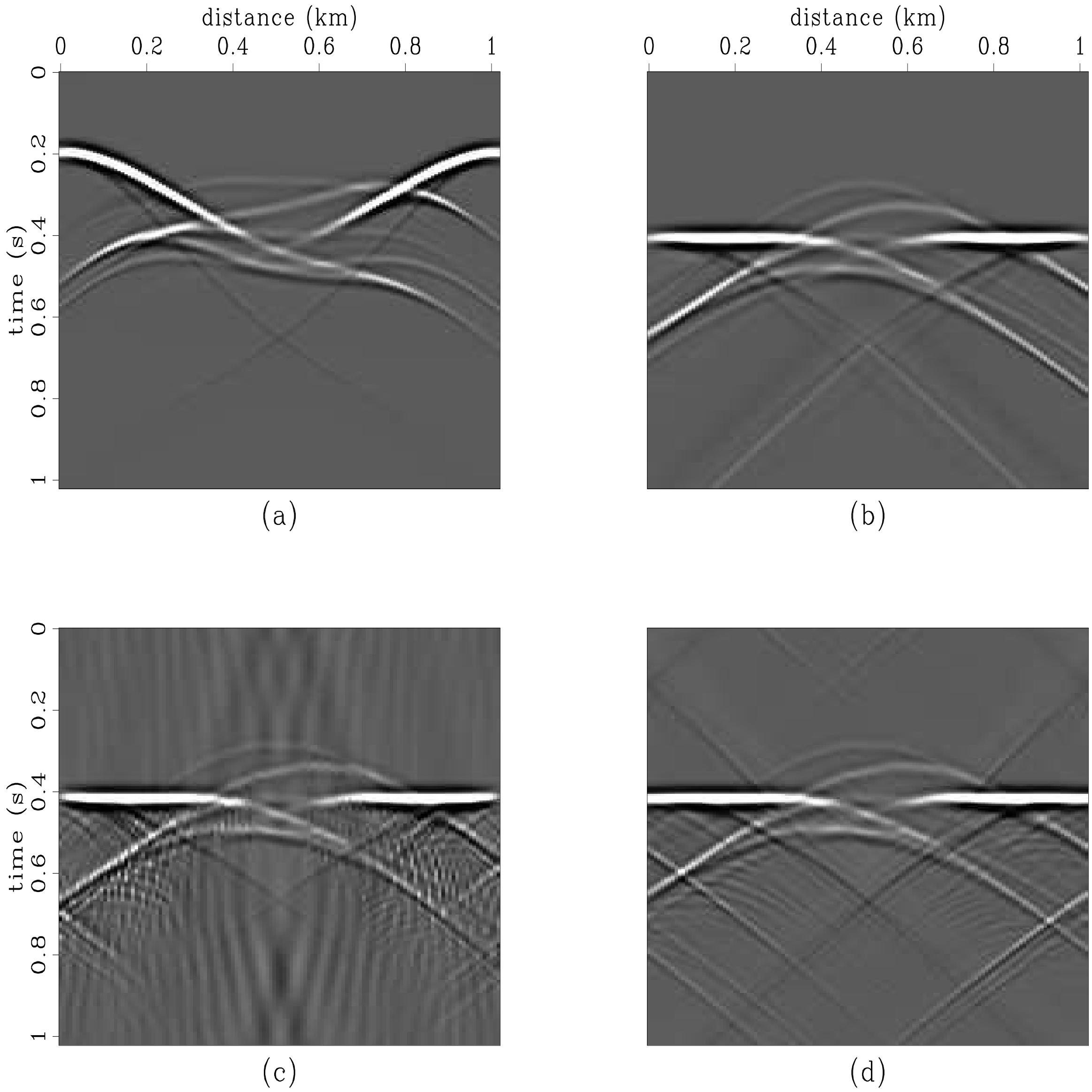

FIG. 2.7. (a) Synthetic data, and upward continuation with (b) Kirchhoff, (c) finite-difference, and (d) phase-shift methods. Operator-datup [CR]

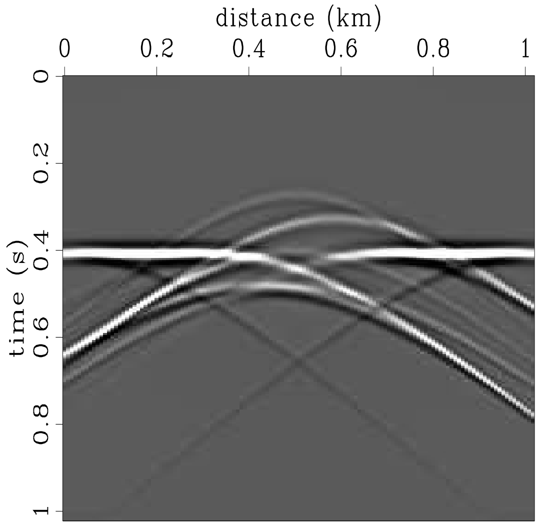

FIG. 2.8. Synthetic data generated at the flat output datum, at an elevation of 210 m. Compare to Figures 2.7b through 2.7d. Operator-syn21 [CR]

rather than propagated off the grid. So, if a phase-shift migration had been used, the high dip resolution would be similar to the Kirchhoff method.

In Chapter 3 I will demonstrate the utility of upward continuing data acquired along a rugged topography to a flat processing datum in order to facilitate wave-based processing and to better determine subsurface velocity.

2.5.2 Downward continuation

In Figure 2.10, the upward continued synthetics of Figure 2.7 have been downward continued back to the original recording surface using the adjoint datuming operators. The Kirchhoff method has most faithfully reproduced the original synthetic. Both the finite-difference and the phase-shift result have a pronounced stair-step effect along the events. This does not occur after upward continuation, but after downward continuation, the discretisation of the topography has introduced an error. This error can be reduced at the cost of a finer grid step size in Δz. Aside from the stair-step effect, both the finite-difference and phase-shift results reasonably restore the original kinematics, although the finite-difference result exhibits more artifacts.

The result of downward continuing the original synthetic (Figure 2.7a) from the topography to a flat datum below the topography with the Kirchhoff algorithm is displayed in Figure 2.11. Downward continuing the data in constant (or depth-variable) velocity does

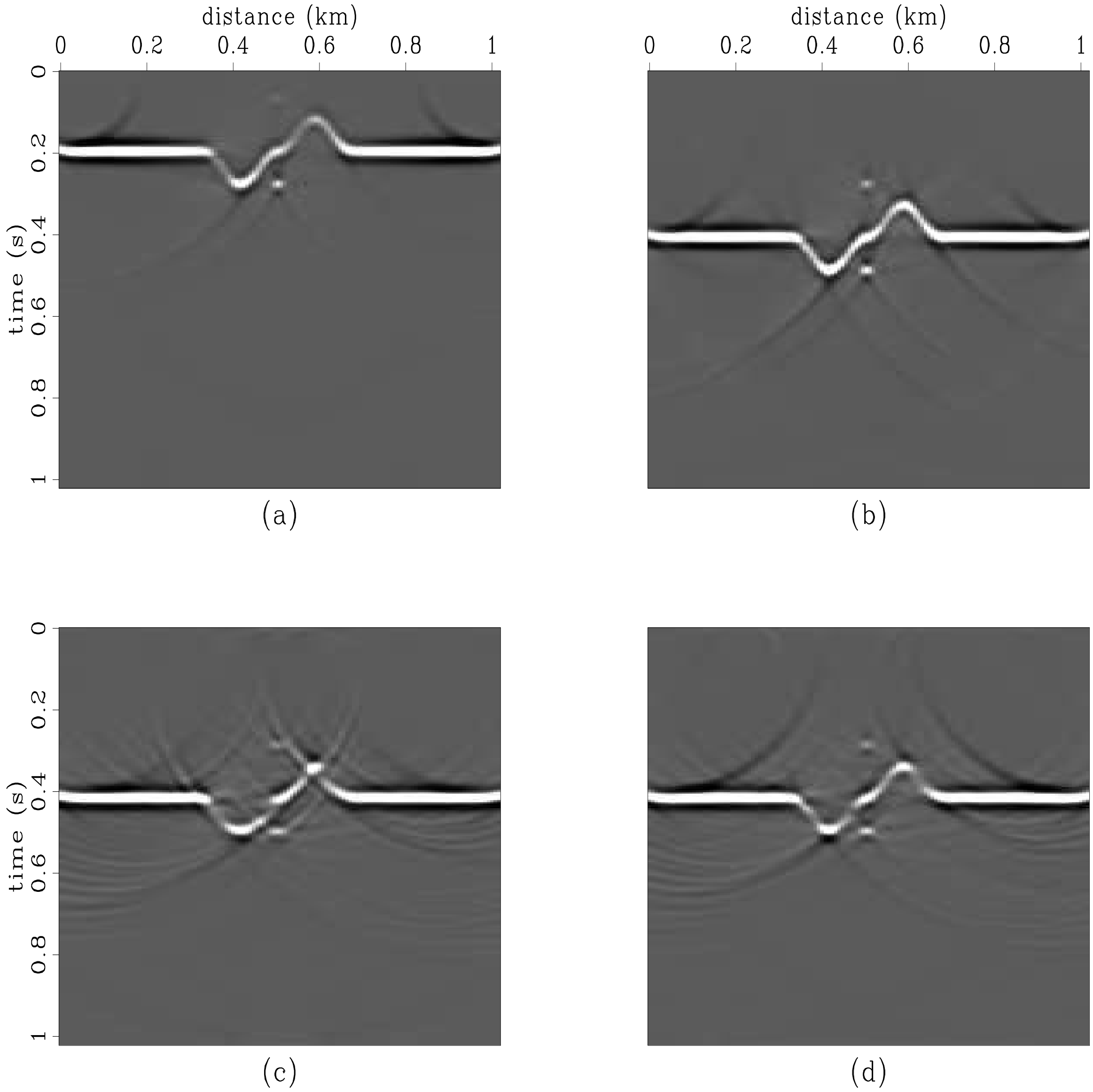

FIG. 2.9. (a) Migration of synthetic data and migration of synthetic data upward continued with (b) Kirchhoff, (c) finite-difference, and (d) phase-shift methods. Operator-datupmig [CR]

not require trace padding because all dip components are propagated downward and inward and the steep dips do not propagate off the computational grid. Therefore, the flanks of the syncline/anticline structure are well imaged without requiring any trace padding.

2.5.3 Near-field vs. far-field Kirchhoff datuming

Figure 2.12 is a comparison of two Kirchhoff upward continuations. In Figure 2.12a the near-field term is retained, and in Figure 2.12b the far-field approximation is made so that equation (2.7) is applied directly. Both results are kinematicly equivalent, but there is a small difference in amplitude and phase behavior, especially for small time shifts τ near the center of the plots where the topography is close to the output datum. The result of migrating Figures 2.12a and 2.12b is presented in Figure 2.12c and 2.12d. There is not much discernible difference between these two plots.

Figure 2.13 shows that as the data are upward continued to a datum that is 100 m above the topography, the amplitude and phase behavior of the near-field and far-field Kirchhoff extrapolations converge. This is further illustrated in Figures 2.14 and 2.15 where traces from two lateral locations are compared after upward continuation with the near-field and far-field Kirchhoff datuming operators. The top traces in Figure 2.14, where the time shift τ is small, exhibit a substantial difference in amplitude and phase. With increasing extrapolation distance, the differences are not as pronounced. In Figure 2.15 I compare two traces at a location where the synthetic wavefield is simpler and where the extrapolation distance is longer because the recording surface is far from the output datum.

From these examples, I conclude that for most cases, the far-field approximation to the Kirchhoff integral is adequate. This is especially true if the data are subject to wave-based processing (in this case, time migration) after datuming. This is significant because it is computationally more efficient to implement Kirchhoff datuming if the near-field term is dropped.

2.5.4 Recursive Kirchhoff continuation

Kirchhoff datuming can be applied recursively, as in the case of finite-difference and phase-shift datuming. This recursive formulation is embodied in equation (2.25), where the W_i operators represent the Kirchhoff extrapolation operator between small depth intervals Δz. Since the depth intervals are small, the time delay τ is short and the computation

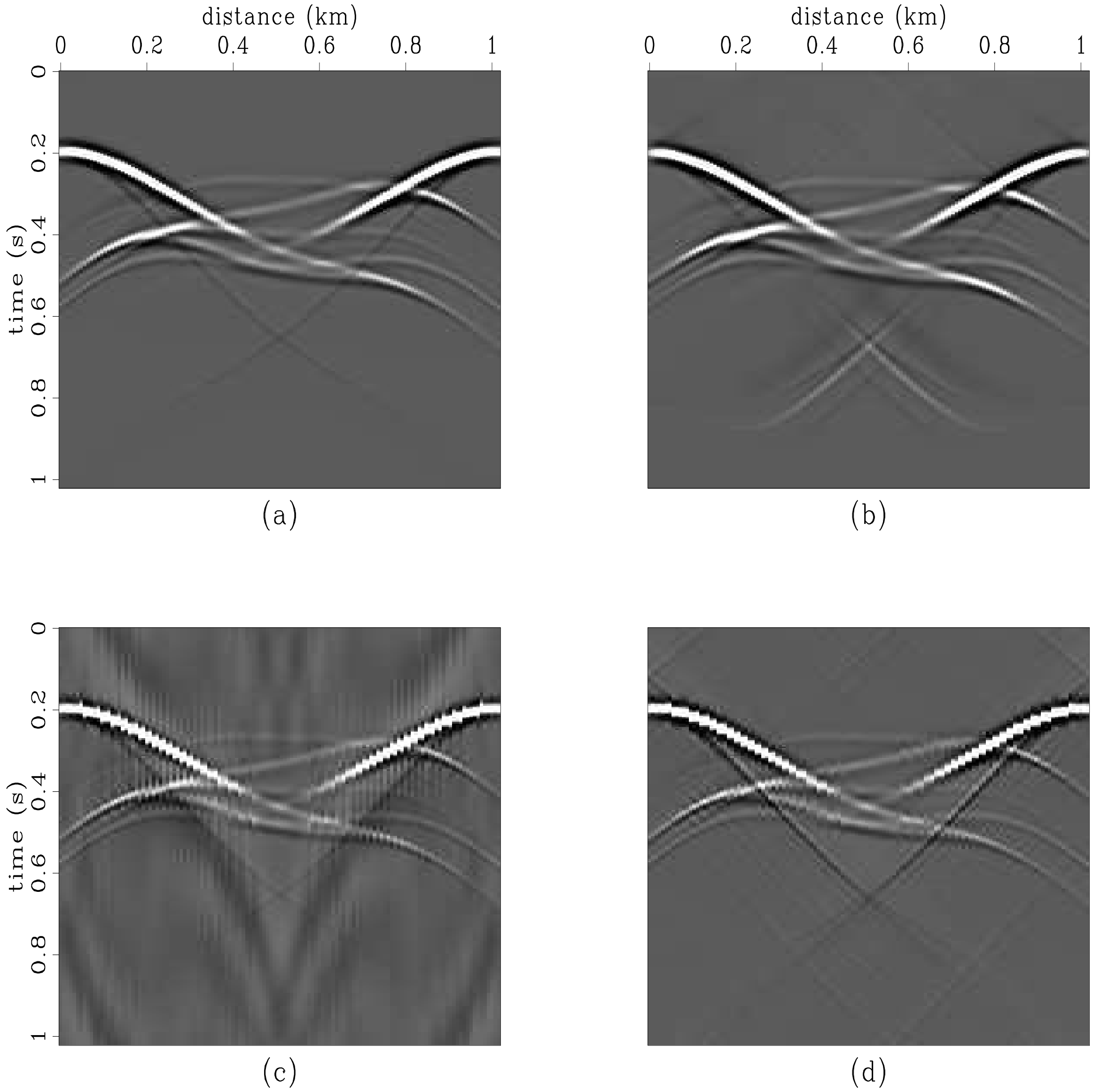

FIG. 2.10. (a) Synthetic data, and downward continuation of the upward continued synthetics from Figure 2.7 with (b) Kirchhoff, (c) finite-difference, and (d) phase-shift methods. Operator-datdn [CR]

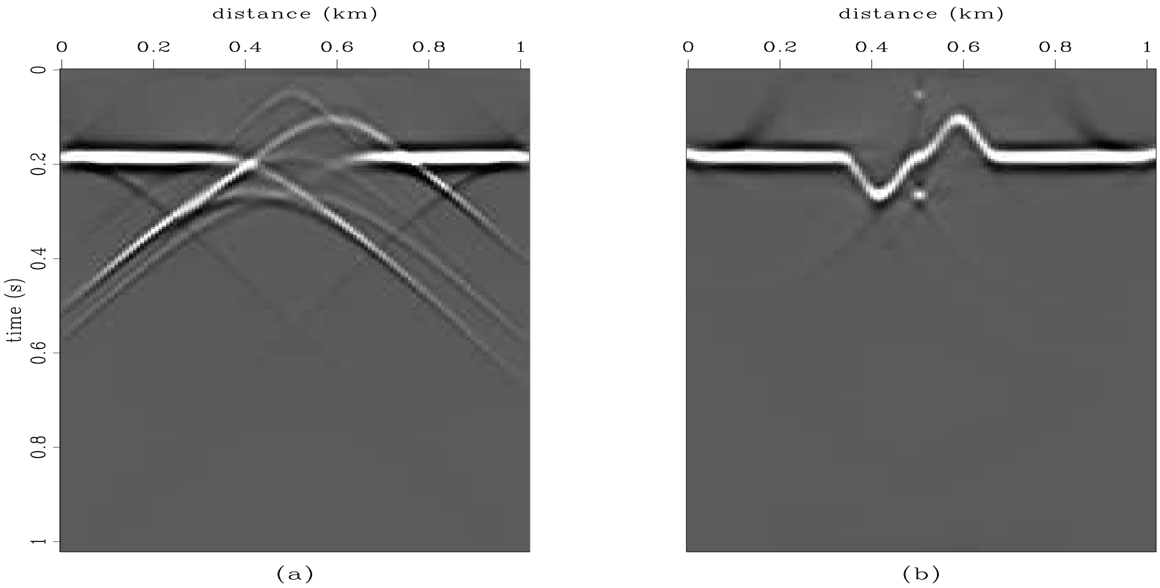

FIG. 2.11. Downward continuation and migration of downward continued synthetic with the Kirchhoff algorithm. Operator-datdnmig [CR]

is definitely in the near field, so it is important to retain the near-field term. Because the extrapolation distance is short, fewer traces can be taken into the integral operator. However, the short extrapolation distance makes the Kirchhoff summation trajectory very steep, necessitating a high degree of operator anti-aliasing for data right at the apex of the summation trajectories. When the depth step is small, the Kirchhoff operator approaches the limit of becoming an explicit finite-difference extrapolator, and all of the difficulties of designing such an operator begin to manifest themselves.

The result of upward continuing the synthetic data with the recursive Kirchhoff datuming algorithm is shown in Figure 2.16. Ten traces were used for every application of the Kirchhoff extrapolator and the same number of depth levels (21) were used as in the phase-shift and finite-difference results. The datuming and migration results are much more low frequency because of the high degree of anti-aliasing required, and the steep dip resolution has decreased because of the limited width of the extrapolator. The migrated image in Figure 2.16b looks more like the image after finite-difference datuming (Figure 2.9c) than after Kirchhoff datuming (Figure 2.9b).

The importance of keeping the near-field term is illustrated in Figure 2.17. When the far-field approximation is made, the recursive extrapolation is overcome by strong artifacts.

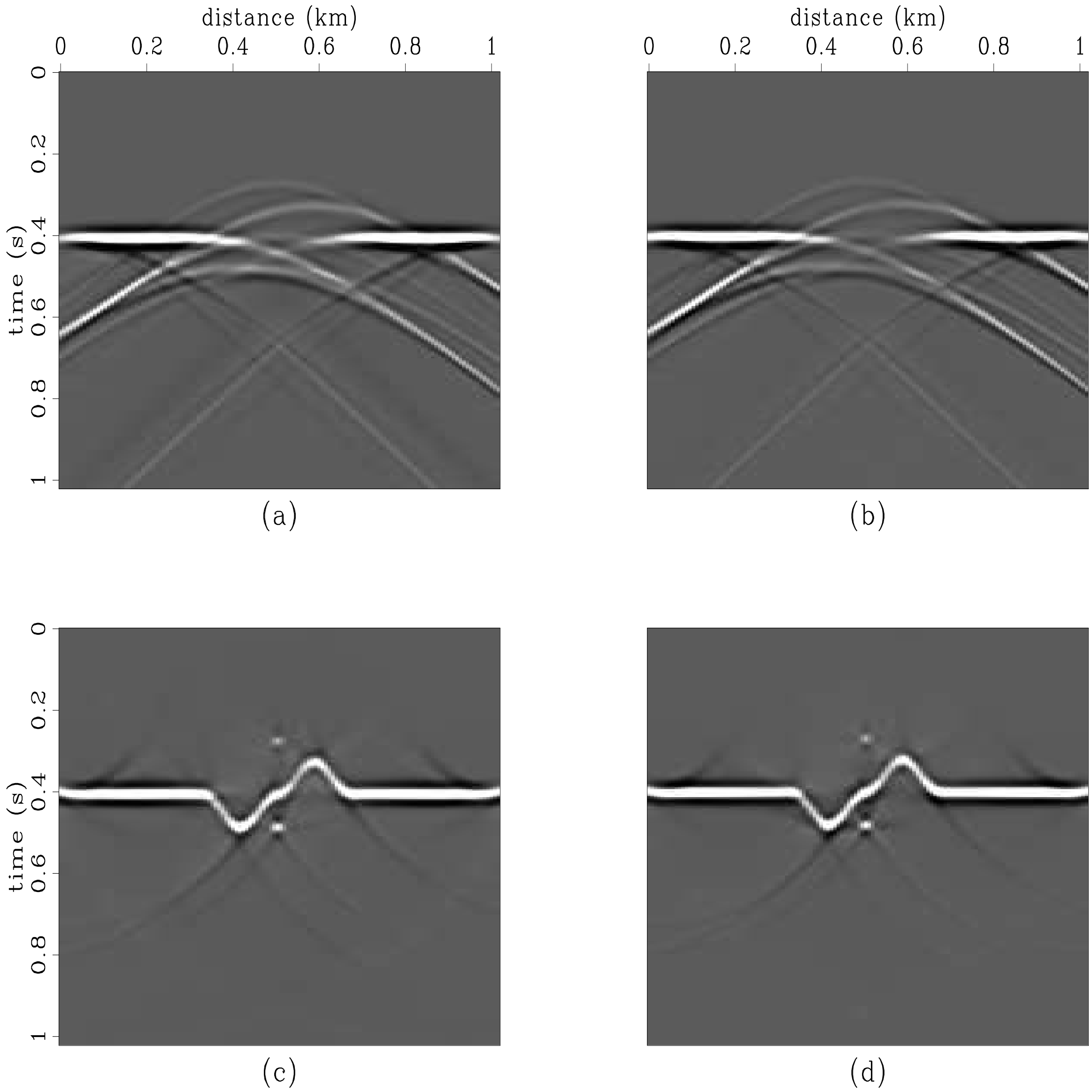

FIG. 2.12. Comparison of (a) near-field Kirchhoff datuming and (b) far-field Kirchhoff datuming. Comparison of migrated (c) near-field Kirchhoff datuming and (d) far-field Kirchhoff datuming. The data have been upward continued to a datum just above the highest topography. Operator-nearvsfar.21 [CR]

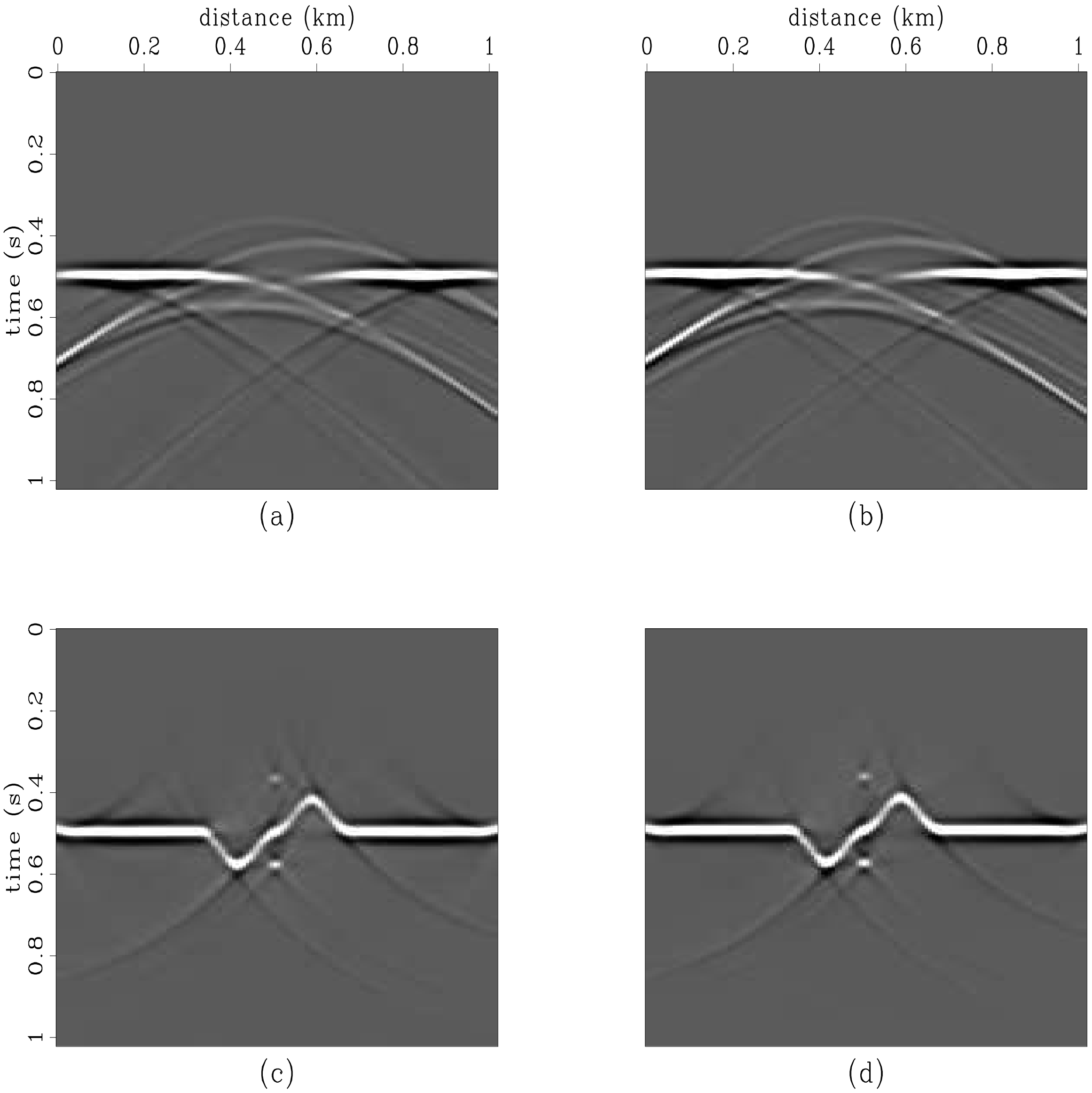

FIG. 2.13. Comparison of (a) near-field Kirchhoff datuming and (b) far-field Kirchhoff datuming. The migrations of the top two panels are presented in c and d. The data have been upward continued to a datum 100 m above the highest topography. Operator-nearvsfar.3 [CR]

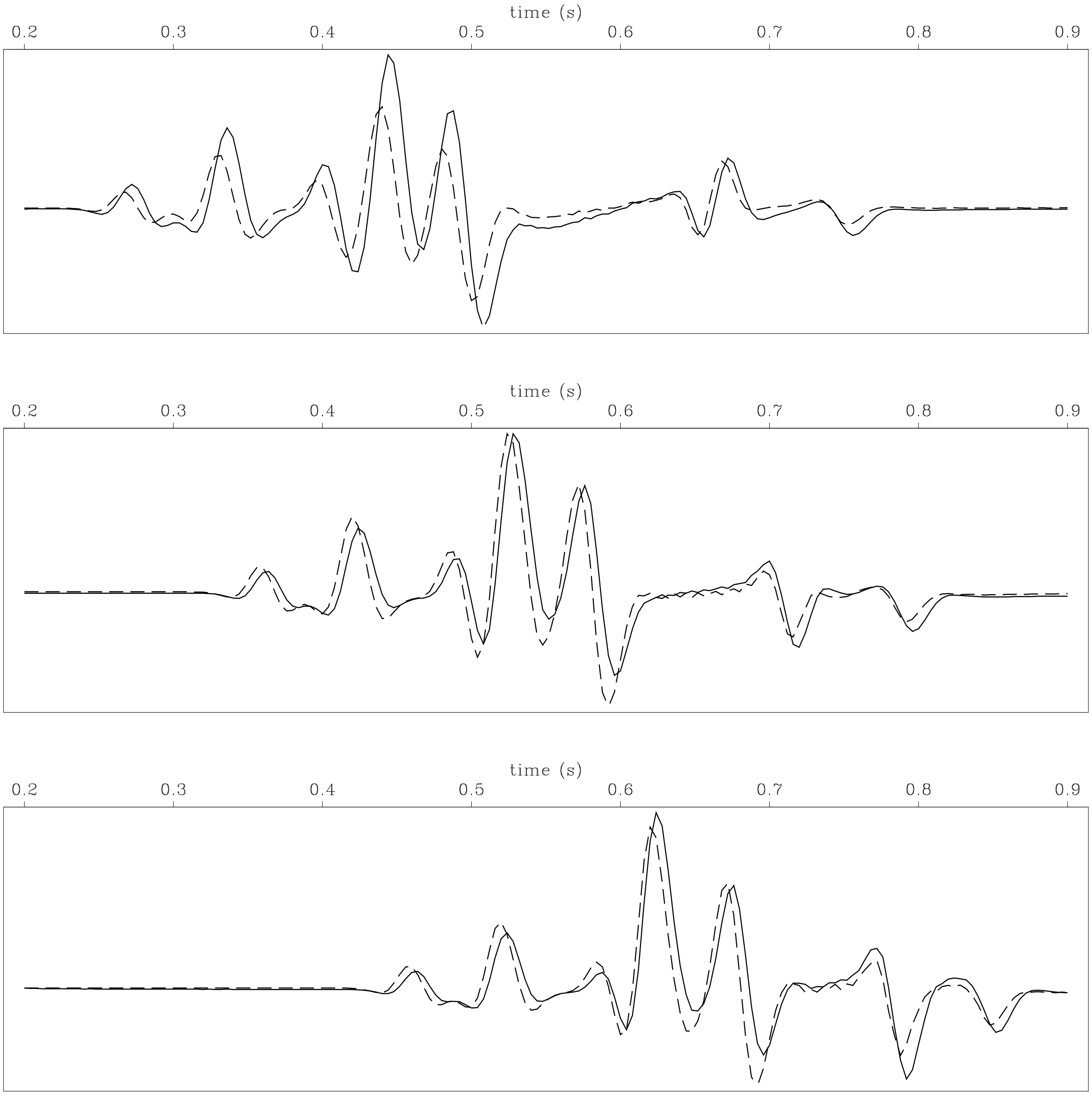

FIG. 2.14. Comparison of traces at horizontal position of 0.5 km for near-field and far-field Kirchhoff datuming. Near-field result is plotted as a continuous line, far-field result is plotted as a dashed line. The plots are for output datum levels of 210 m (top), 300 m (middle), and 400 m (bottom). $\boxed{\text{Operator-diffnfmid}}$ [CR]

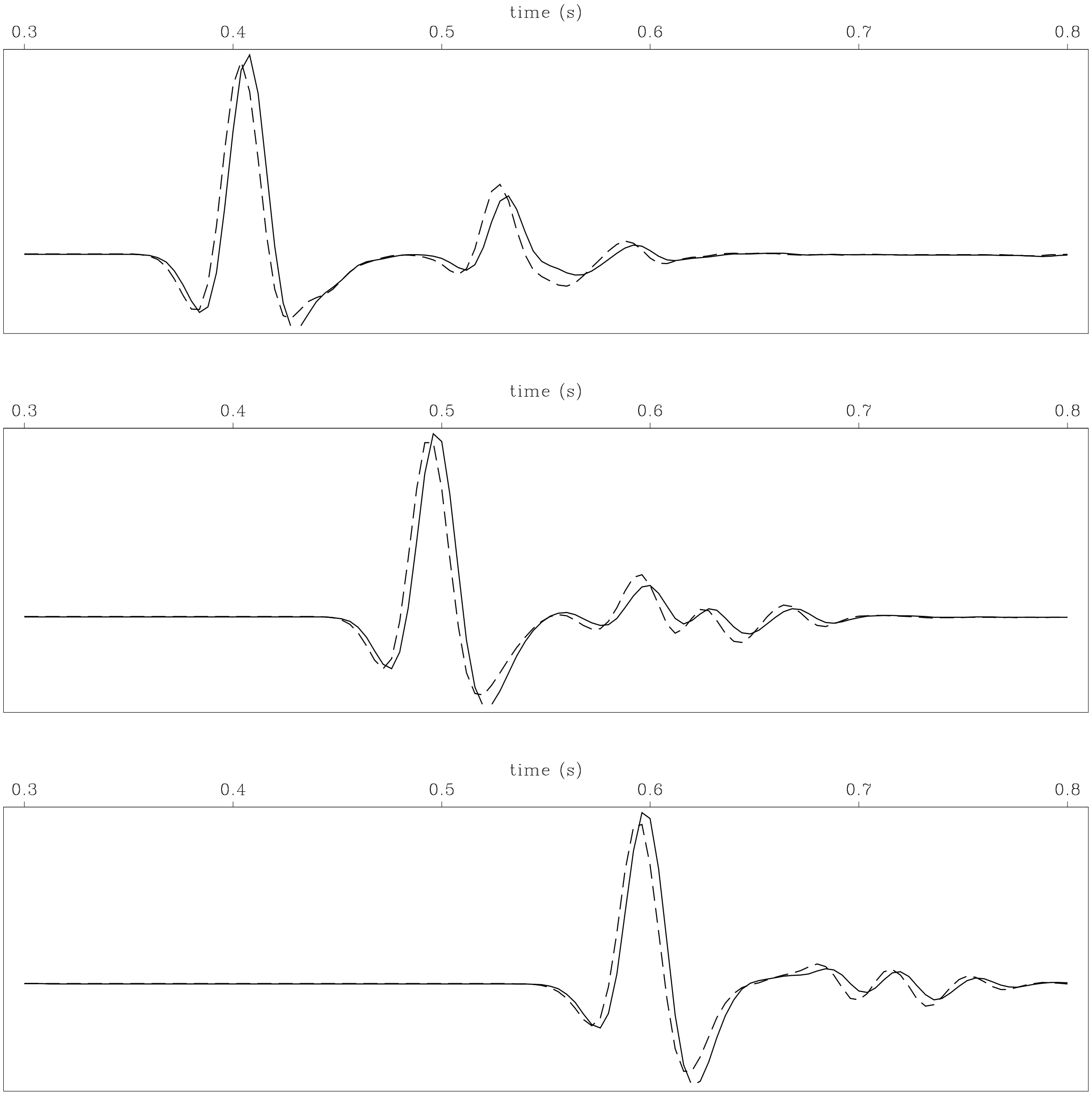

FIG. 2.15. Comparison of traces at horizontal position of 0.25 km for near-field and far-field Kirchhoff datuming. Near-field result is plotted as a continuous line, far-field result is plotted as a dashed line. The plots are for output datum levels of 210 m (top), 300 m (middle), and 400 m (bottom). Operator-diffnfside [CR]

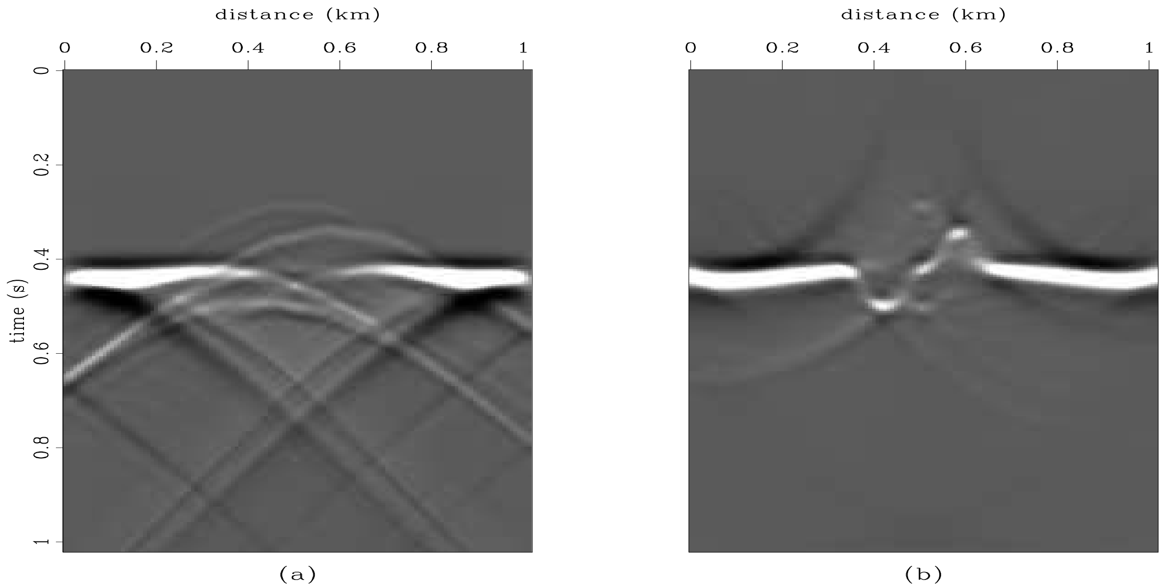

FIG. 2.16. (a) Recursive Kirchhoff datuming and (b) migration of the recursively redatumed synthetic. Operator-recursive [CR]

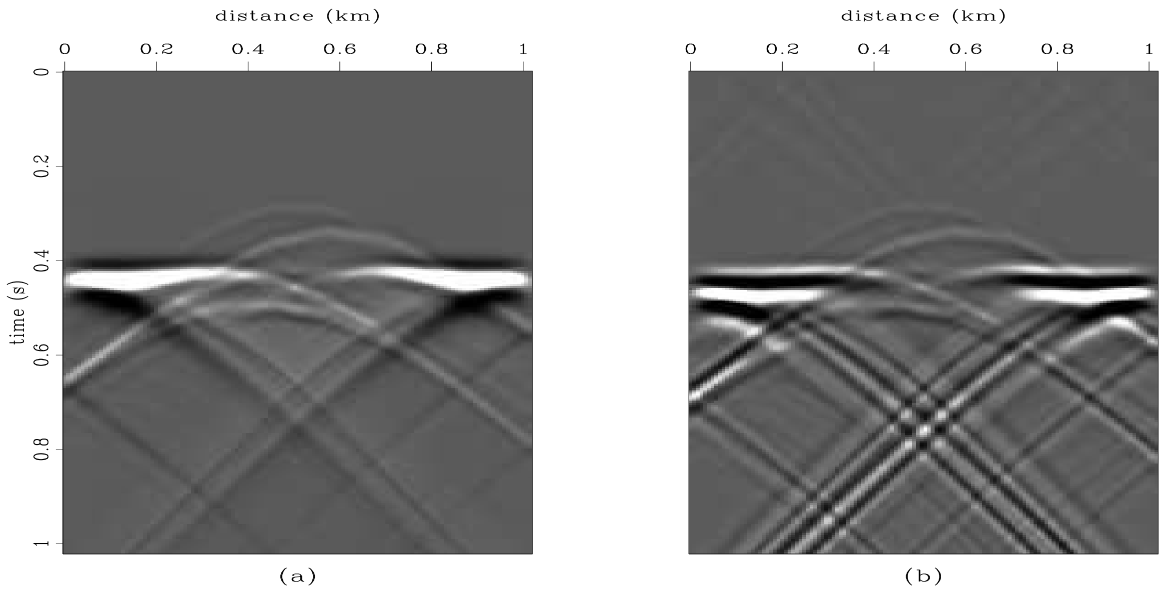

FIG. 2.17. Illustration of the importance of including the near-field term in recursive Kirchhoff extrapolation. (a) When the near-field term is included, the extrapolation is successful, (b) when the far-field approximation is made, the recursive extrapolation is dominated by artifacts. Operator-stab [CR]

The recursive Kirchhoff extrapolator results in poorer results than any of the aformentioned methods and is very inefficient computationally. I have presented it merely to demonstrate how the datuming methods can be linked. In practice there are much more efficient methods of recursive explicit extrapolation.

2.6 Comparison of datuming operators

All three of the formulations presented can accommodate lateral velocity variation. The chief drawback of the recursive methods is that they require a regular computational grid. The grid must be sampled with a sufficient vertical density so that the topography can be adequately discretized; otherwise, artifacts are introduced. The synthetic results show that Kirchhoff datuming produces the best output. But more importantly, it is the most efficient method for application to prestack data, and it can be easily applied to 3-D data. Furthermore, the Kirchhoff implementation handles the exact topographic elevations, not some discretized representation. The Kirchhoff method is not confined to a regular grid, so for the irregular geometries of land data acquired in rugged terrain and for 3-D implementation considerations, the datuming algorithm based on the Kirchhoff integral is the operator of choice.

In the remainder of this dissertation, I will demonstrate how the Kirchhoff datuming operator can be applied to improve imaging in two of the most challenging environments facing geophysicists: overthrust areas with substantial surface topography and areas of complex velocity structure.